Chemosphere 313 (2023) 137368

Contents lists available at ScienceDirect

Chemosphere

journal homepage: www.elsevier.com/locate/chemosphere

Fate of antimony contamination generated by road traffic – A focus on Sb geochemistry and speciation in stormwater ponds

M. Philippe [a,b], P. Le Pape [b,*], E. Resongles [c], G. Landrot [d], R. Freydier [c], L. Bordier [a], B. Baptiste [b], L. Delbes [b], C. Baya [b], C. Casiot [c], S. Ayrault [a]

[a] Laboratoire des Sciences du Climat et de l'Environnement (LSCE-IPSL), UMR 8212 (CEA/CNRS/UVSQ), Université Paris-Saclay, Gif-sur-Yvette, France
[b] Institut de Minéralogie, de Physique des Matériaux et de Cosmochimie (IMPMC), UMR 7590 CNRS – Sorbonne Université – IRD – MNHN, 4 place Jussieu, 75252 Paris, Cedex 5, France
[c] HydroSciences Montpellier (HSM), Université de Montpellier - CNRS - IRD, Montpellier, France
[d] Synchrotron SOLEIL, F-91192 Gif-Sur-Yvette, France

HIGHLIGHTS

- Highway stormwater ponds concentrate Sb contamination from road runoff.
- Sb isotopic composition of stormwater pond sediments is close to that of road dusts.
- Sb(V)–O, Sb(III)–O, and Sb(III)–S species occur in the road-to-pond continuum.
- Sb(III)–S species are observed as a specific signature of underwater reduced samples.
- Sb speciation changes along the waterway show the high geochemical reactivity of Sb.

GRAPHICAL ABSTRACT

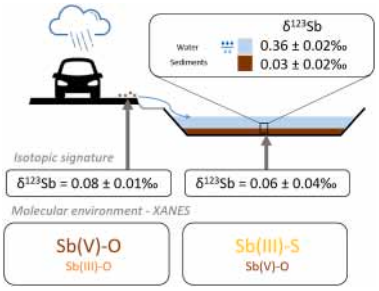

ARTICLE INFO

Handling Editor: Milena Horvat

Keywords:
Antimony
Road traffic contamination
Stormwater ponds
Sb isotopes
Sb speciation
Pb isotopes

ABSTRACT

Although antimony (Sb) contamination has been documented in urban areas, knowledge gaps remain concerning the contributions of the different sources to the Sb urban biogeochemical cycle, including non-exhaust road traffic emissions, urban materials leaching/erosion and waste incineration. Additionally, details are lacking about Sb chemical forms involved in urban soils, sediments and water bodies. Here, with the aim to document the fate of metallic contaminants emitted through non-exhaust traffic emissions in urban aquatic systems, we studied trace element contamination, with a particular focus on Sb geochemistry, in three highway stormwater pond systems, standing as models of surface environments receiving road-water runoff. In all systems, differentiated on the basis of lead isotopic signatures, Sb shows the higher enrichment factor with respect to the geochemical background, up to 130, compared to other traffic-related inorganic contaminants (Co, Cr, Ni, Cu, Zn, Cd, Pb). Measurements of Sb isotopic composition (δ^{123}Sb) performed on solid samples, including air-exposed dusts and underwater sediments, show an average signature of 0.07 ± 0.05‰ ($n = 25$, all sites), close to the δ^{123}Sb value measured previously in certified reference material of road dust (BCR 723, $\delta^{123}Sb = 0.03 \pm 0.05$‰). Moreover, a fractionation of Sb isotopes is observed between solid and dissolved phases in one sample, which might result from Sb (bio)reduction and/or adsorption processes. SEM-EDXS investigations show the presence of

* Corresponding author. Institut de Minéralogie, de Physique des Matériaux et de Cosmochimie (IMPMC), UMR 7590 CNRS – Sorbonne Université – IRD – MNHN, 4 place Jussieu, 75252 Paris, Cedex 5, France.
E-mail address: pierre.le-pape@cnrs.fr (P. Le Pape).

https://doi.org/10.1016/j.chemosphere.2022.137368
Received 29 August 2022; Received in revised form 9 November 2022; Accepted 21 November 2022
Available online 26 November 2022

discrete submicrometric particles concentrating Sb in all the systems, interpreted as friction residues of Sb-containing brake pads. Sb solid speciation determined by linear combination fitting of X-Ray Absorption Near Edge Structure (XANES) spectra at the Sb *K*-edge shows an important spatial variability in the ponds, with Sb chemical forms likely driven by local redox conditions: "dry" samples exposed to air exhibited contributions from Sb(V)–O (52% to 100%) and Sb(III)–O (<10% to 48%) species whereas only underwater samples, representative of suboxic/anoxic conditions, showed an additional contribution from Sb(III)–S (41% to 80%) species. Altogether, these results confirm the traffic emission as a specific source of Sb emission in surface environments. The spatial variations of Sb speciation observed along the road-to-pond continuum likely reflect a high geochemical reactivity, which could have important implications on Sb transfer properties in (sub)surface hydrosystems.

1. Introduction

Global-scale antimony (Sb) contamination has been recorded in ice cores since the early 1900s (Krachler et al., 2005; Liu et al., 2021). In particular, the increase in Sb concentrations has been interpreted as a rise of anthropogenic inputs related to waste incineration and mining (Krachler et al., 2005; Liu et al., 2021). At the urban scale, different sources contribute to the Sb biogeochemical cycle, including non-exhaust road traffic emissions, urban materials leaching/erosion and waste incineration (Filella et al., 2009). In the urban Orge River basin (Paris region, France), an increase in Sb enrichment factors (EFs) in river suspended particulate matters (SPM) has been persistently observed along the increasing urbanization gradient (Le Pape et al., 2012; Froger et al., 2018). In Budapest (Hungary), Sb atmospheric contamination has been observed in urban aerosols, showing extreme enrichment factors, from 5,097 in PM_{10} to 18,892 in PM_2, and were interpreted as resulting from road traffic (Salma and Maenhaut, 2006). Indeed, road traffic is known to induce emissions of inorganic contaminants due for instance to abrasion of brake pads (Von Uexküll et al., 2005; Napier et al., 2008), namely copper (Cu), zinc (Zn), cadmium (Cd), chromium (Cr) and Sb. In particular, Sb has been used in brake pads lubricants (Sb_2S_3) as replacement for asbestos (Chan and Stachowiak, 2004; Lee et al., 2013). Additionally, metallic trace element emissions are also reported as originating from tires and oils combustion or leakage (Hjortenkrans et al., 2007; Davis et al., 2001; Johansson et al., 2009) and other urban materials such as safety barriers, road paints or cigarette butts (Zhang et al., 2004; Moriwaki et al., 2009; Kibblewhite, 2018; Turner and Filella, 2020). After their emission at the road scale, these contaminants are transported by road runoff and potentially impact the quality of surface waters (Helmreich et al., 2010; Le Pape et al., 2012; Wang et al., 2017; Froger et al., 2018). Although traffic is generally mentioned as a major source of Sb in the urban environment (Hjortenkrans et al., 2006; Johansson et al., 2009), its contribution to the global urban Sb contamination is poorly quantified. Nonetheless, identification of the contributions of the diverse sources and pathways of Sb contamination could lead to a better management of this pervasive and persistent geochemical enrichment, for instance by adapting public policy to control or remove part of these contamination sources.

Highway stormwater ponds, located along roads, are recognized as efficient accumulators of road contaminations since they directly receive the runoff water leaching roads and other surfaces contaminated by vehicles-related emissions (Hares and Ward, 1999; Clozel et al., 2006; Hwang et al., 2016). Additionally, as some of these stormwater pond systems are vegetated, and harbour sedimentary systems representative of urban soils and sediments, they stand as interesting model hydrosystems (Stachel et al., 2010) to study the mechanism of Sb accumulation from road emissions. While Cu, Zn, Cd, Cr and Pb concentrations from measurements in road and street dusts are often reported in the literature (*e.g.* Ahmed and Ishiga, 2006; Haus et al., 2007), Sb enrichment and chemistry have rarely been studied in road-related environments, in particular in such stormwater pond systems. A few data are currently available for road ponds, and only focusing on Sb contamination level based on the measurements of its concentrations in bulk and dissolved fractions of pond water samples from Germany, England, Sweden and Canada (up to 11 $\mu g.L^{-1}$ (Kamalakkannan et al., 2004; Stachel et al., 2010; Nielsen et al., 2015; Perron and Pick, 2020)) and in sediments from a UK motorway drainage pond (1.44–2.01 $mg\,kg^{-1}$) (Kamalakkannan et al., 2004). However, neither speciation nor isotopic measurements are currently available on these accumulating pond system media, data which could be extended to surface media exposed to road emissions such as urban areas in general.

To study the sources and the transfer pathways of contaminant-bearing particles, the relative abundance in contaminant isotopes in both the aqueous and the solid phases has proven to be an informative geochemical parameter (Monna et al., 1997). For instance, in urban context, $^{208}Pb/^{206}Pb$ *vs.* $^{206}Pb/^{207}Pb$ ratios have been used as anthropogenic source tracers in soils (Emmanuel and Erel, 2002), or to estimate the urban pressure exerted on urban rivers (Ayrault et al., 2012; Le Pape et al., 2013). Indeed, Pb is a common and abundant contaminant of urban environments, whose isotopic composition allows discriminating between natural and anthropogenic sources for lead-bearing particles (Ayrault et al., 2012). Comparatively, Sb isotopic signature has been scarcely used in the literature, and has never been used to trace Sb contamination in the urban context. The pioneering study of Rouxel et al. (2003) gives the first values of Sb fractionation between ^{123}Sb and ^{121}Sb for different natural samples representative of diverse sources at the Earth surface, including seawater and main geological rocks. This study also suggests that Sb isotopic fractionation could be a useful tracer for biogeochemical processes affecting Sb, such as changes in oxidation state. More recently, in environmental sciences, $\delta^{123}Sb$ has been used to trace the contributions from different Sb sources in mine-impacted streams (Resongles et al., 2015b). Thus, Sb isotopic signature has a good potential for both discriminating the sources of Sb at the site scale and could also help to trace the local biogeochemical processes involving changes of oxidation state, ligand exchange, or adsorption onto natural particles (Ferrari et al., 2022; Zhou et al., 2022).

Determining the physico-chemical processes governing Sb mobility in surface environments is essential to unravel the transfer pathways leading to the dissemination of this toxic metalloid. As Sb is a redox sensitive element, Sb mobility is strongly driven by its speciation in both the aqueous and the solid phases. In (sub-)surface soils and sediments, Sb harbours two oxidation states, Sb(III) and Sb(V), the latter form presenting the higher solubility (Johnston et al., 2020). Thus, determining Sb speciation is of prime importance to predict Sb short-to long-term transfer properties. Currently, the few information on Sb speciation have been obtained *via* chemical extractive methods applied to road soils, road dusts, and airborne particles (Amereih et al., 2005; Quiroz et al., 2013; Sánchez-Rodas et al., 2017), showing various contributions from both Sb(III) and Sb(V) species. Varrica et al. (2013) have measured Sb speciation *via* X-ray Absorption Spectroscopy (XAS) at the Sb *K*-edge in various urban particles, and observed a mix of Sb(V)–O, Sb (III)–O and Sb(III)–S molecular environments, interpreted as directly resulting from brake pad friction and abrasion (Cho et al., 2006; Martinez and Echeberria, 2016). Thus, a full comprehensive description of Sb speciation along the road-to-pond continuum is necessary to determine whether Sb speciation is inherited from direct traffic inputs or can be further influenced by local biogeochemical processes taking place in

surface soils and sediments.

Here, we have compared the level of trace metal contamination, including Sb, in three stormwater pond systems along roads presenting high traffic volumes in the Ile-de-France region (France). These sites are considered as model systems representative of surface environment accumulating the contaminations from road traffic, which can be largely found in urban areas (*e.g.* urban hydrosystems, rivers, wetlands). Additionally, the studied sites are representative of different land uses (rural and urban) and of different chronologies of dust and sediment deposition. Both sediments and waters were sampled in the road-to-pond continuum, with the aim to reveal the spatial evolution of trace element contamination from emission to deposition in near road environments. Thanks to a combination of techniques, including contaminant concentration analyses (among them Cu, Cd, Cr, Ni, Pb, Sb, Zn), analysis of relative abundance of Pb and Sb isotopes, and speciation analysis of Sb, we highlight key steps of Sb biogeochemical cycle in surface environments impacted by road traffic. Thus, we show that the level and type of contamination of pond systems are likely related to the nature of drained surfaces (urban *vs.* rural) and extent of particle accumulation. Then, we identified a specific δ^{123}Sb signature of highway stormwater pond samples, including road dusts and sediments, which is shown to be close of that reported elsewhere for road dust. Finally, we studied in detail the variations of Sb speciation by the mean of XANES at the Sb *K*-edge in solid samples along the road-to-pond continuum, showing that Sb presents an important geochemical reactivity, with multiple oxidation states and ligands involved as a function of the local redox conditions.

2. Materials and methods

2.1. Study sites

The three highway stormwater pond systems studied are located in the south of Île-de-France region in the Orge River watershed (Fig. SI-1.1). Previous researches performed in the Orge River basin have provided a good knowledge of land use, geology, spatial and temporal dynamics of contaminants of anthropogenic origin (*e.g.* metals and PAHs) (Le Pape et al., 2012; Froger et al., 2018, 2019). The highway stormwater pond systems studied are different by the nature of drained areas (urban + road, mostly road or 100% road) but also by their design (decantation pond, filtration pond, presence or not of a polyethylene geomembrane) and their construction date (Table 1). Road sections related to the studied stormwater ponds have a high daily flux of ~50, 000 vehicles per day (Table 1). The presence of speed cameras near both semi-urban systems should be noted because it induces braking and therefore potentially additional emission of dust due to abrasion of brake pads. Three systems are studied: recent semi-urban (SUR) situated in Orsay, old semi-urban (SUO) situated in Marcoussis, and recent rural (RR) situated near Saint-Martin-de-Bréthencourt. Fig. 1 represents the spatial organization of the three stormwater pond systems. The SUR system is composed by 3 geomembrane isolated ponds arranged in series and connected by rafts at their base and by nozzles in height for overflows during important rain events. The first pond (B1) is located upstream and the third (B3) downstream. Both B1 and B2 are planted with reeds while B3 is channeled and unplanted. A "natural pond" (P) supplied by the upperlying aquifer of the Fontainebleau sands (W), independent of the road runoff collection network but hydrologically connected to B3, is also present. The SUO system is composed by 2 disconnected unplanted decantation ponds situated in an urban area surrounded by crops. The "A" pond had been dredged a few days before sampling while "B" pond has never been dredged since the pond construction (Fig. 1). The RR system is divided in two sub-sites: "Direction 1" (1A10) composed by a geomembrane isolated decantation pond planted with reefs in series with a dry filtration pond, and "Direction 2" (2A10) composed by two systems of unplanted geomembrane isolated decantation ponds in series with dry filtration ponds. Waters from both sub-sites come from the road through a spillway system.

2.2. Sampling

Sediments (S), concrete downhill crusts (CDC), road dust sediments (RDS), water samples (dissolved fraction (W) and suspended particulate matters (P)) were sampled during the five sampling campaigns carried out in January (2 campaigns) and February 2020 for SUR and SUO systems and March and September 2020 for the RR system.

Underwater sediments were collected in 180 mL polypropylene containers tightly closed onsite and a water column was kept above the sediments to avoid direct contact with air. Such reduced sediments were then inserted as quickly as possible in a glove box at the IMPMC laboratory for further sample processing. Inside the glove box, the solid samples were separated from the liquid phase by centrifugation, dried under vacuum, and finally stored in anoxic conditions (N_2, <5 ppm O_2). Dissolved fraction of the water samples was recovered by filtering to 0.22 µm with PES filters (Sartorius Minisart™) and acidified with ultrapure nitric acid (0.5 M) in 50 mL Falcon® tubes directly on site and further stored at 4 °C. Bulk water (~2 L) was collected in PE bottles previously washed with HNO_3 0.5 N and rinsed on site with bulk water. Water pH, conductivity and temperature were measured onsite except for 2 samples in the RR pond system (15 water samples listed in Table SI-1.2). Road dust sediments (RDS) were collected on the road using a plastic spatula and placed in a tightly closed polyethylene bag (SUO system) or using a plastic brush and kept in a Falcon tube® (SUR system). Crusts were collected on the slope concrete tiles channeling water from the road to the pond with a plastic spatula and kept in a tightly closed polyethylene bag. RDS and crusts were stored at room temperature in the dark. Full information about the 41 solid samples (conditions of sampling, drying conditions, type and matrix) are listed in Table SI-1.1.

2.3. Sample preparation

2.3.1. Suspended particulate matter (SPM) and sediment

Within the hours following collection, SPM samples were obtained by filtration (in laboratory) of approximatively 2 L of bulk water (sometime less when clogging occurred) through previously dried and weighted quartz filters (Pallflex® Tissuquartz™, retaining 99.9% of >0.3 µm particles) using glass or plastic tulips previously rinsed with 0.5 N nitric acid and a pump. The filtered volume was measured by weighting. After filtration, filters were dried under oxic conditions before total mineralization (Priadi et al., 2011). For multi-elemental

Table 1
Characteristics of the highway stormwater pond systems (year of construction, type of pond conception, type of drained surfaces, traffic intensity and presence of speed cameras).

Denomination	GPS coordinates	Construction (year)	Type	Drained surface	Trafic per day (2017)	Presence of speed camera
Semi-urban, recent (SUR)	48.7115, 2.1863	~2000	Decantation	Urban + Road	54,187	Yes
Semi-urban, old (SUO)	48.6334, 2.2246 48.6320, 2.2292	1990s	Decantation	Road	56,595	Yes
Rural, recent (RR)	48.5120, 1.9072 48.5125, 1.9082	2012	Decantation + filtration	Road	42,225	No

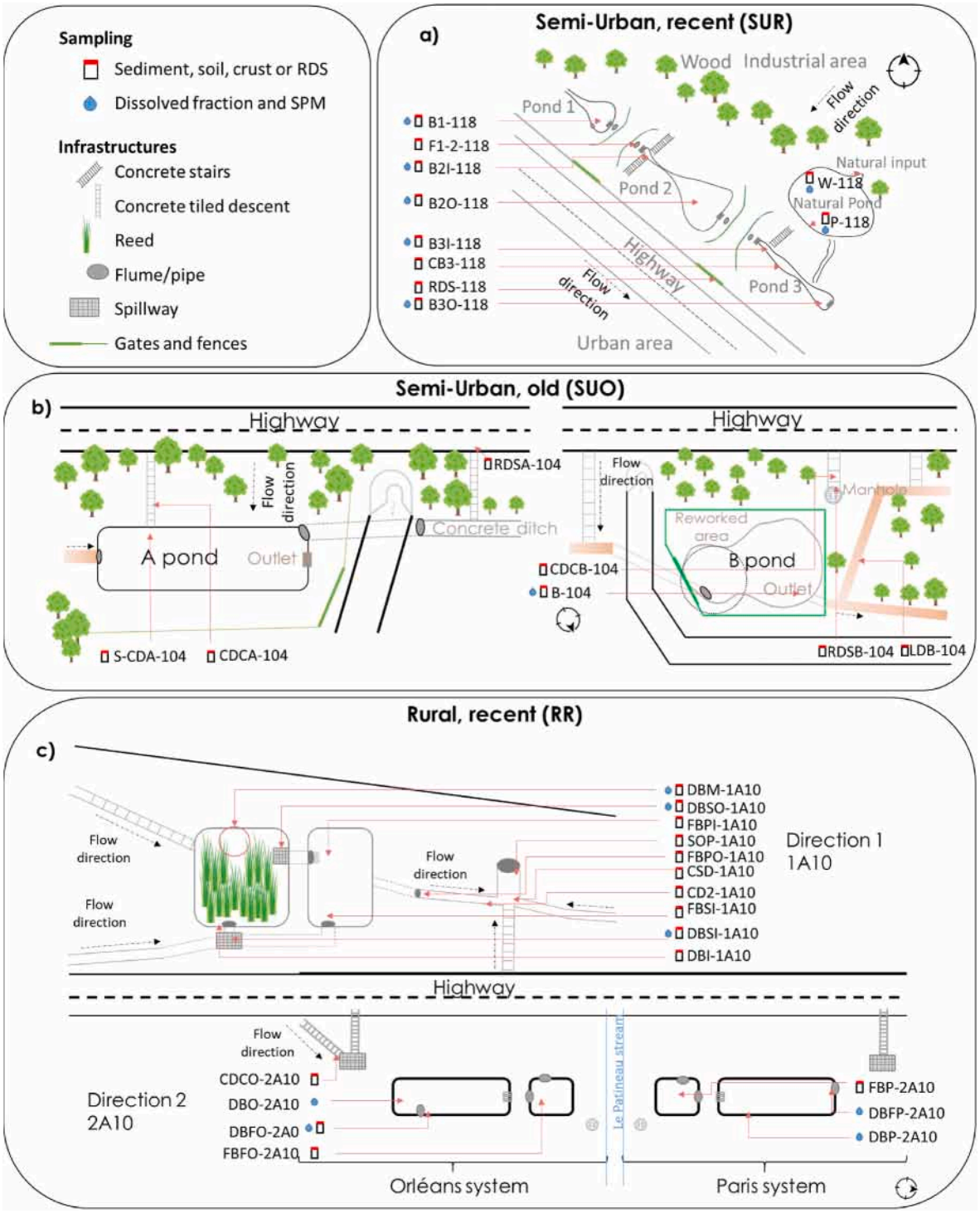

Fig. 1. Layout of the three studied stormwater pond systems. (a) Semi-Urban Recent system (SUR) of Orsay, (b) Semi-Urban Old system (SUO) of Marcoussis and (c) Rural Recent system (RR) of Saint-Martin-de-Bréthencourt. Sampling locations for each type of samples (water, SPM, sediment) are indicated on the schemes. Pots symbols stand for solid sampling. Drops stand for water sampling (dissolved phase, <0.22 μm) and suspended particulate matters (SPM >0.3 μm) sampling.

analysis, approximately 100 mg of sediment, previously sieved at 2 mm with a plastic sieve, were crushed in an agate mortar before total mineralization (Le Pape et al., 2012).

2.3.2. *Bulk mineralization*

Total digestion of sediments and SPM was performed in three steps using ultrapure concentrated acids to avoid contaminations in open PTFE Savillex® vials: 4 mL of HF (47–51%) and 2 mL $HClO_4$ (67%) heated at 150 °C for 320 min, 3.75 mL of HCl (34–37%) and 1.25 mL of HNO3 (67%) heated at 120 °C for 180 min and finally heating at 110 °C with addition of 1 mL of HNO3 (67%) for 55 min. Final solutions were transferred to 50 mL Falcon® (polyethylene) tubes, Savillex® vials rinsed three times by heating approximatively 10 mL of HNO_3 0.5 M and completed at 50 mL with 0.5 M nitric acid (Le Pape et al., 2012). Two certified reference materials (CRM), sediment SL1 and street dust BCR 723, were added in each mineralization batch. Blanks were performed in

each batch and a filter blank was included in each SPM batch.

2.4. Analytical methods

2.4.1. Elemental analysis and enrichment factors calculation

The concentrations of 25 major, minor and trace elements were determined using triple quadrupole inductively coupled plasma – mass spectrometry (TQ-ICP-MS) (Thermo Scientific™ iCAP™ TQ) at LSCE laboratory (Tables SI-1.3, SI-1.4, SI-1.5). An internal standard mixture (In, Ge, Rh and Re) was added on-line to the samples to correct for the instrumental sensitivity drift. Quality of analysis was checked using NIST 1640a (spring water) for dissolved samples, SL1 and BCR-723 for sediments (100 mg) and for SPM (10 mg) (Table SI-1.6). Accuracy was within ±15% of the certified values provided for the certified reference material SL1 and BCR 723 (except Ag: 19%). The relative standard deviation (RSD) for SPM are higher (<32%): measured concentrations were close to quantification limits due to the low mass of SPM recovered on filters.

Enrichment Factors (EF) are classically used to determine the contamination level of solid samples (Salma and Maenhaut, 2006; Le Pape et al., 2012; Froger et al., 2018). EFs are calculated as a comparison of the Al-normalized trace element concentration in the sample with the local background values (Equation (1)).

$$EF = \frac{\frac{X_{Sample}}{Al_{Sample}}}{\frac{X_{Background}}{Al_{Background}}} \quad (1)$$

With X_{Sample} and $X_{Background}$ the concentrations of the element under consideration in the sample and its geochemical background, and Al_{Sample} and $Al_{Background}$ the aluminum concentrations in the sample and in the geochemical background. Local background determined for the Orge River catchment for Sb (Froger et al., 2018) and for the Seine River for Al, Cd, Cr, Cu, Ni, Pb and Zn (Thévenot et al., 2007) were used to calculate the EFs. Full set of elemental concentrations and associated EFs are shown in Table SI-1.7. Details on the use and calculations of enrichment factors according to the interpretation of Sutherland (2000) are given in the supplement information section.

2.4.2. Radiogenic lead isotope ratio analysis

Radiogenic lead isotopic ratios ($^{206}Pb/^{207}Pb$ and $^{208}Pb/^{206}Pb$) were measured by TQ-ICP-MS in solid samples previously mineralized and diluted to obtain a Pb concentration of 2 µg.L^{-1} in solution. In order to control mass bias and/or instrument drift, an isotopic Pb reference material, NIST NBS 981, was measured every two samples. To control measurement accuracy, the mineralized CRM SL1 was measured multiple times with the samples and the results were compared to the data 1.217 ± 0.008 in $^{206}Pb/^{207}Pb$ and 2.037 ± 0.003 in $^{208}Pb/^{206}Pb$ published by Farmer et al. (2002). SL1 measurements were in the margins of errors. More methodological details are given in supplementary information (SI-3) and the results are shown in Table SI-1.8. Briefly, lead isotope ratio signature was used as tracer for contaminant sources to study the nature of sediment inputs in each pond system (Komárek et al., 2008) using the published isotopic signature of the potential local sources of Pb (Fig. SI-3.1; Table SI-1.8), *i.e.* the local urban Pb end-member, the local Pb geochemical background, and the French leaded gasoline.

2.4.3. Antimony isotopic composition analysis

An aliquot of water samples and mineralized solutions of solid samples containing 50–100 ng of Sb underwent a purification step on TSP cartridges (thiol-functionalized mesoporous silica powder) in order to separate Sb from the other chemical species and to preconcentrate it in low-concentrated samples according to the method detailed in Ferrari et al. (2021). For each batch of purification, a certified reference material (BCR 723, Table SI-1.9) and a blank was included. Blanks contribution represented less than 0.8 ng of Sb (<1.6%). Antimony isotopic composition of the samples were then analysed by HG-MC-ICP-MS (Hydride Generation coupled to a Multi-Collector Inductive Coupled Plasma Mass Spectrometer, Neptune+, Thermo Fisher Scientific) on the AETE-ISO platform (OSU OREME, University of Montpellier), using instrument parameter settings given in Ferrari et al. (2021). A sample-standard bracketing approach was used to correct the mass bias. An in-house isotopic Sb standard solution (SPEX CertiPrep (Sb 1000 µg mL^{-1} in 20% w/w HCl, batch number 24-175SBX)) was analysed before and after every sample. The isotopic composition of Sb was expressed according to equation (2) which represents the deviation between the isotope ratio measured for the sample and the mean isotope ratio of the in-house isotopic standard (SPEX) measured before and after the sample. Detailed results are presented in Table SI-1.9.

$$\delta^{123}Sb(‰) = \left(\frac{\left(\frac{^{123}Sb}{^{121}Sb}\right)_{sample} - \left(\frac{^{123}Sb}{^{121}Sb}\right)_{mean\ std}}{\left(\frac{^{123}Sb}{^{121}Sb}\right)_{mean\ std}} \right) \times 1000 \quad (2)$$

Antimony isotopes could help in determining the transfer pathways of Sb contamination by tracing the contributions of distinct sources (Rouxel et al., 2003). Sb isotopes data have mainly been determined in mine-affected environments and river waters ($\delta^{123}Sb = -0.06‰$ to $+0.83‰$) (Resongles et al., 2015a), in environmental references samples (Rouxel et al., 2003; Ferrari et al., 2021; Sun et al., 2021; Wang et al., 2021), and in ancient glass materials (Lobo et al., 2013; Degryse et al., 2015; Dillis et al., 2019). Here, this tool is applied for the first time to road-affected surface environmental samples in an attempt to trace the contributions of distinct Sb sources, which could help in determining the transfer pathways of Sb contamination.

2.4.4. Powder X-ray diffraction (XRD)

Powder XRD diffractograms were obtained on a Panalytical™ Xpert pro® diffractometer in the Bragg-Brentano geometry using Co *K*α radiation to minimize Fe X-ray fluorescence. Samples were previously crushed in an agate mortar to obtain a fine powder. Bragg reflexions were indexed using the Highscore Plus® software associated to the PDF 2 database (2020). To check for potential sample oxidation, test samples were first measured within an anaerobic chamber and results were compared to those obtained without the chamber. As no changes were observed in XRD data for underwater anoxic test samples, the whole set of samples was consequently analysed under oxic conditions. Reference compounds of ferrihydrite co-precipitated with Sb(V) or Sb(III), synthesized for X-Ray absorption measurements at the Sb *K*-edge (see supplementary information SI-2 for synthesis details), were analysed by X-Ray diffraction and Wide angle X-ray Scattering associated to Pair distribution function analysis on the CRISTAL beamline at SOLEIL.

2.4.5. Scanning electron microscopy coupled with energy dispersive X-ray spectroscopy (SEM-EDXS)

SEM investigation associated to punctual EDXS analysis was performed on non-crushed samples embedded in resin to conserve the aggregate structure of particles at the microscopic scale. SEM-EDXS analyses were performed at IMPMC, with a GEMINI ZEISS™ Ultra55 Field Emission Gun Scanning Electron Microscope equipped with a Bruker™ Si-drift detector for EDXS acquisition. Prior to analysis, bulk samples were embedded in an epoxy resin (Epoxy, Presi™) and polished. Polished sections samples were coated with carbon before SEM observation. EDXS spectra were performed on specific spots on the surface of samples using the esprit 1.9 or 2.2 software.

2.4.6. X-ray absorption spectroscopy at the Sb K-edge

To examine the potential changes of Sb chemical forms along the road-to-pond continuum, X-Ray Absorption Spectroscopy Near Edge Structure (XANES) measurements were performed on the solid samples. Given the large shifts in energy between different types of molecular

environments and ligands at the Sb *K*-edge (typically 4 eV between maxima for Sb(V)–O and Sb(III)–O, and 2 eV between maxima for Sb (III)–O and Sb(III)–S), XANES measurements classically allow the quantification of the different species in samples of unknown speciation, namely the contributions of Sb(V)–O, Sb(III)–O, and Sb(III)–S (Bennett et al., 2017; Arsic et al., 2018; Burton et al., 2020). Hereafter in the text, in the section concerning speciation by XANES at the Sb *K*-edge, the samples are labelled as "Dry" when they were sampled as dried powders on the field and as "Underwater" when they were collected under a column of water and kept under anoxic conditions until analysis. The single "Wet" sample was collected as wet and dried at the laboratory under oxic conditions.

2.4.6.1. Synthesis of reference compounds, sample preparation and data sampling. Ferrihydrite coprecipitated with Sb(III) and Sb(V) (Fh-Sb(III) or Fh-Sb(V)), tripuhyite ($FeSbO_4$) and amorphous antimony trisulphide (Sb_2S_3) were synthesized to serve as reference compounds. Details on the synthesis protocols can be found in the supplement information section (SI-2). Sb_2O_3 was purchased from Sigma Aldrich. For reference compounds, an appropriate amount of sample was diluted into cellulose and pressed in pellets for transmission measurement when possible. For Fh-Sb samples, spectra were also measured in transmission mode. For environmental samples from stormwater ponds, pure sample pellets were prepared by pressing approximately 50 mg of finely ground sample in a Jacomex™ glove box ($O_2 < 4$ ppm). All pellets were covered with Kapton® tape and transported to the synchrotron facility in anoxic containers according to proven protocols (Le Pape et al., 2017).

Antimony *K*-edge X-ray absorption spectroscopy data were collected in both transmission and fluorescence detection modes at 80 K in a liquid azote cryostat on the bending magnet SAMBA beamline at SOLEIL Synchrotron (Gif-sur-Yvette, France). Fluorescence signals were measured using a Canberra™ 36-elements Ge array detector and incoming beam energy was monitored through a Si (220) double-crystal monochromator. Data were calibrated using a Sb foil at 30,491 eV at the maximum of the first derivative of the XANES spectrum. Samples were mounted on PEEK sample holders in a Jacomex™ glove box at IMPMC and onsite. Sample holders were immersed in liquid N_2 for the transfer to the beamline cryostat. Because Sb concentrations in samples were less than 100 mg kg^{-1}, a minimum of 25 quick scans were necessary to obtain a good signal to noise ratio for each natural sample.

2.4.6.2. Data processing and analysis. The FASTOSH program (Landrot, 2018) was used to calibrate and normalize Sb *K*-edge extended X-Ray absorption near edge structure data and to proceed to background subtraction. A linear combination fitting (LCF) analysis was performed on the XANES spectra on the first derivative of the absorption to determine the relative contributions of Sb(V)–O, Sb(III)–O and Sb(III)–S species in the stormwater pond samples. To do so, the Fh-Sb(V), Fh-Sb (III), and am-Sb_2S_3 references compounds were considered as the most relevant to perform the LCF analysis. LCF accuracy on derivative of XANES spectra were estimated by a R-factor (Equation (3)) and reduced chi-square (Equation (4)):

$$R-factor = \frac{\sum_{p=1}^{t}[data(p)-fit(p)]^2}{\sum_{i=1}^{m}[data(p)]^2} \quad (3)$$

$$\chi_R^2 = \frac{1}{(t-s)}\sum_{i=1}^{t}[data(i)-fit(i)]^2 \quad (4)$$

With "data" designating the experimental spectrum, "fit" the spectrum reconstructed by LCF, "p" a specific point in each spectrum, "t" the total number of points in each spectrum, "i" an independent data point corresponding to a specific independent measurement and "s" the number of reference spectra considered in fit. The statistical criteria considered for the introduction of a new fitting component was the significant decrease of the reduced chi-square.

3. Results

3.1. Radiogenic lead isotope ratios in solid samples

The detailed results of lead isotope ratio analysis are shown in the Supplementary information (SI-3). The recent rural stormwater pond system (RR) signatures are distributed along a mixing line between the leaded gasoline and the local geochemical background endmembers. Lead isotope ratios measured in the SUR and SUO pond systems fall on the same mixing line but the range of variations is smaller and isotopic signatures are close to the urban lead endmember. Extreme value close to the gasoline endmember is measured for the S-DBSI-1A10 sample collected at the entry pond spillway (RR), *i.e.* located directly at the entrance of the pond system receiving road runoff. The closest value to the geochemical background signature is observed for the sediment sample S–P-118, which is located in SUR system natural freshwater pool receiving water from the overlaying Fontainebleau sand aquifer. Accordingly, this sample presents a particularly low Pb concentration (16 mg kg^{-1}), confirming that this part of the system is not collecting road traffic runoff.

3.2. Analysis of highway stormwater pond contamination: spatial variation of elemental geochemistry and enrichment factors

Dissolved Sb concentrations (Table SI-1.5) range from 0.26 µg.L^{-1} (W–P-118) to 12.5 µg.L^{-1} (W–W-118) in the SUR pond system and from 0.27 µg.L^{-1} (W-DBFP-2A10) to 13.2 µg.L^{-1} (W-DBSI-1A10) in the RR pond system. The only dissolved sample available in the SUO system shows a concentration of 0.90 µg.L^{-1} (W-DBFP-2A10).

Concentrations of trace elements in sediments, RDS and crusts samples range between 9.8 and 103 mg kg^{-1}, <3.5–48 mg kg^{-1}, 8.5–895 mg kg^{-1}, 40–2,539 mg kg^{-1}, 0.2–3.2 mg kg^{-1}, 0.5–93 mg kg^{-1} and 8.2–444 mg kg^{-1} for Cr, Ni, Cu, Zn, Cd, Sb and Pb respectively (Table SI-1.3). The corresponding EFs calculated in sediments, RDS and crusts samples are shown in Fig. 2a. In the RR system, Co, Cr, Ni, Cd and Pb are not specifically enriched ($EF \leq 5$). However, EF of Cu and Zn indicate a significant contamination level ($1 \leq EF \leq 19$). In the SUO system, mean enrichment contamination levels of Co, Cr and Ni are not significant ($EF \leq 3$). Zinc, Cd and Pb enrichment contamination level is classified as "significantly enriched" ($2 \leq EF \leq 29$) and Cu enrichment contamination levels are very strongly enriched (EF up to 99). In SUR system, Cu enrichment contamination levels reach very strong values (up to 26) and extreme values are occasionally observed for Zn ($EF = 63$ in RDS-118). In the three studied stormwater pond systems, Sb is extremely enriched with respect to the local geochemical background, with maxima EF values as high as 119 in RR (S-FBPI-1A10), 130 in SUO (CDCA-104) and 103 in SUR system(S–F1_2–118), attesting of important inputs of Sb in this urban area. It is noteworthy that the Sb natural abundance is low, with a local geochemical background of 0.2–0.5 mg. kg^{-1} (Froger et al., 2018). Therefore, the Sb geochemical anomaly induced by anthropogenic Sb emissions in this urban context is particularly prominent (as reflected by extreme EFs values), this trend has already been observed in other large cities (Chen et al., 2008; Gonzalez et al., 2016; Dong et al., 2017; Nory et al., 2021).

In comparison with sediments, SPM is a dynamic component in this type of system. Metal concentrations (Table SI-1.4) and EFs (Fig. 2b) in SPM have been quantified to give a picture of contamination transfer by surface particles. Concentrations of trace elements in SPM samples range between 44 and 186 mg kg^{-1}, 18–57 mg kg^{-1}, 51–985 mg kg^{-1}, 168–5,019 mg kg^{-1}, 0.6–10 mg kg^{-1}, 2–83 mg kg^{-1} and 24–738 mg kg^{-1} for Cr, Ni, Cu, Zn, Cd, Sb and Pb respectively. As observed for sediments, Co, Cr and Ni are not particularly enriched in RR and SUR systems (Fig. 2b). In contrast, Cu, Zn and Sb are significantly enriched in RR and SUR systems. Cadmium is also significantly enriched in SUR system while only moderately enriched in RR system sediments. Lead is moderately enriched in RR and SUR systems sediments. Again,

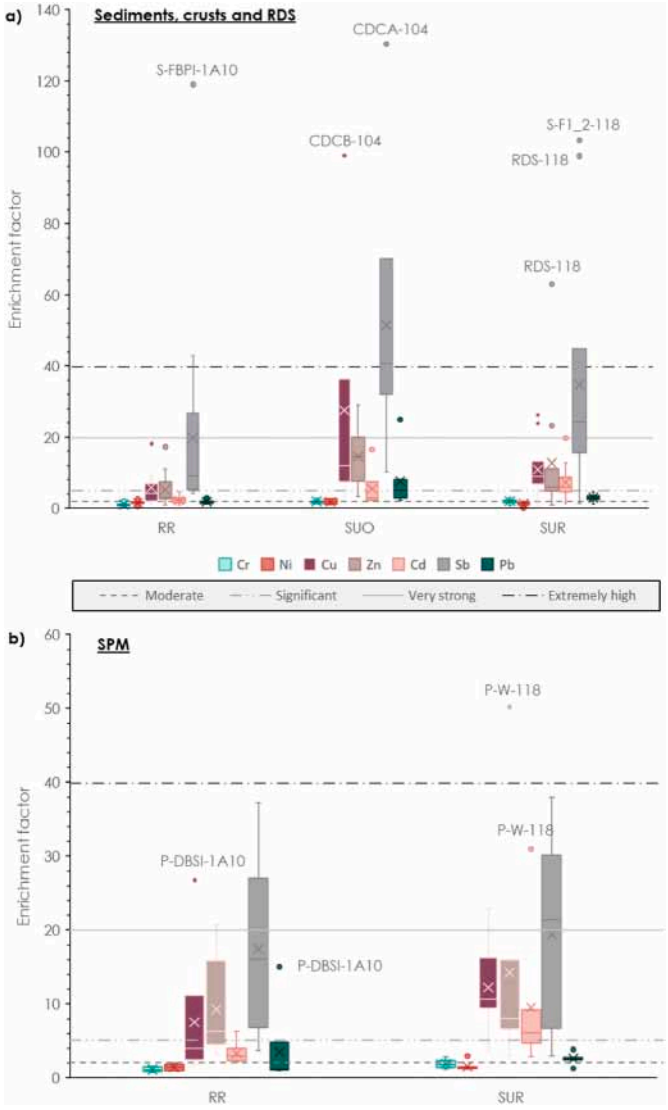

Fig. 2. Aluminium-normalized enrichment factors for a) sediments, soil, RDS and crusts and b) SPM samples compared to the local geochemical background (Thévenot et al., 2007; Froger et al., 2018). Chromium EF are shown in cyan, Ni in red, Cu in purple, Zn in taupe, Cd in pink, Sb in grey and Pb in green. Eighteen samples are considered for constructing the box plot in the RR system, 7 for SUO system, 10 for SUR system. Six samples are considered for SPM in RR system and 7 in SUR system. The bottom branch of each boxes represents the minimum value, the bottom of the box represents the first quartile, the horizontal line inside the box represents the median value, the cross represents the mean value, the top of the box represents the third quartile, the dots represent extreme values and the top of the branch represents the maximum value for series without extreme values. Horizontal lines indicate the level of enrichment according to the classification of Sutherland (2000). (For interpretation of the references to colour in this figure legend, the reader is referred to the Web version of this article.)

Sb presents the highest mean EF values in SPM in both RR and SUR systems sediments. Otherwise, two punctual very high EFs values are observed in the RR system for the sample P-DBSI-1A10 at 27 for Cu and 21 for Zn. In the SUR system, extreme values are determined for the sample P–W-118 at 50 for Zn and 31 for Cd. EFs determined in SPM of the RR and SUR systems are comparable between both ponds while their EFs are different in sediments.

The Cu/Sb ratio is frequently used in literature to trace the brake pad contamination in areas impacted by road traffic (*e.g.* Stechmann and Dannecker, 1990). Indeed, these two elements are important constituents of brake pads (Dong et al., 2017). In our study, the local geochemical background can be estimated at Cu/Sb = 25 (Sb concentration from Froger et al. (2018) and Cu from Thévenot et al. (2007)). In the SUR system, Cu/Sb reach up to 39 in S–W-118 (natural pond) and down to 6 in RDS-118, with an average of 12, and 9 if the two samples from natural pond are excluded (S–W-118 and S–P-118). SUO system Cu/Sb values are between 6 (RDSB-104) and 35 (CDCB-104) with an average of 12. In RR system the Cu/Sb values are situated between 4 (S-FBPI-1A10) and 21 (CD2-1A10) with an average of 9.

3.3. Analysis of Sb sources using δ^{123}Sb isotopic signatures

Measurements of antimony isotopes are applied for the first time to road-affected surface environmental samples in an attempt to trace the contributions of distinct Sb sources, which could help in determining the transfer pathways of Sb contamination. Fig. 3a and b present δ^{123}Sb values as a function of 1/[Sb] for solid and liquid samples, respectively. Antimony isotopic compositions of solid samples measured at the three sampling sites range from 0.02 ± 0.02‰ to 0.22 ± 0.03‰ with an average of 0.07 ± 0.05‰ (n = 25). No significant variation of the average δ^{123}Sb values was observed between the sampling sites ($\delta^{123}Sb_{SUO} = 0.06 \pm 0.02$‰ (n = 7); $\delta^{123}Sb_{SUR} = 0.06 \pm 0.04$‰ (n = 13), excluding the two samples of the natural pond); $\delta^{123}Sb_{RR} = 0.09 \pm 0.05$‰ (n = 3)). On average, values observed for the sediments are closer from those reported by Ferrari et al. (2021) for the certified reference material of Austrian RDS (BCR 723, δ^{123}Sb = 0.03 ± 0.05‰) than from both Netherlands incinerator fly ash (BCR 176R, δ^{123}Sb = -0.03 ± 0.03‰) and low-density polyethylene (ERM-EC 680 m, δ^{123}Sb = 0.40 ± 0.03‰). Taken individually, road deposit sediment (RDS) samples from the SUO and SUR pond systems, represented in red on the zoom part of Fig. 3a, present δ^{123}Sb values and 1/[Sb] values relatively close from those of the BCR 723 (Austrian RDS collected in an urban tunnel), with δ^{123}Sb = 0.07 ± 0.04‰ for RDS-118, 0.08 ± 0.06‰ for RDSA-104 and 0.09 ± 0.02‰ for RDSB-104.

Two samples of the SUR system highlighted in green in Fig. 3a present the highest δ^{123}Sb values (0.18 ± 0.04‰ for S–W-118 and δ^{123}Sb = 0.22 ± 0.03‰ for S–P-118), associated with low Sb concentrations close to the geochemical background (0.51 mg kg^{-1} and 0.57 mg kg^{-1}). These samples are interpreted as not directly impacted by road emission, which is consistent with lead isotope ratio data (see SI-3). In SUR system, five sediment samples taken in a 15 cm core sampled every 3 cm in the B3 SUR basin (Fig. 1) show a decreasing concentration in Sb as a function of depth in the core (19.4 mg kg^{-1} for S-CB3-0_3–118 and 1.35 mg kg^{-1} for S-CB3-12_15–118) with a concomitant slight increase of δ^{123}Sb values from 0.02 ± 0.02‰ to 0.04 ± 0.06‰ for 0–9 cm depth and from 0.09 ± 0.02‰ to 0.13 ± 0.06‰ for 9–15 cm depth.

For water samples from the RR system, δ^{123}Sb ranges from 0.12 ± 0.03‰ to 0.36 ± 0.02‰ with an average of 0.19 ± 0.09‰ (n = 5). Thus, dissolved Sb presents an enrichment in heavy Sb isotope compared to particulate Sb (average $\delta^{123}Sb_{RR} = 0.09 \pm 0.05$‰, n = 3). Interestingly, at the DBSO sampling point, corresponding to a spillway separating the settling and filtration ponds, a strong difference between the δ^{123}Sb signatures of the sediments and the dissolved phase is observed: 0.03 ± 0.02‰ and 0.36 ± 0.02‰, respectively. This indicates a significant fractionation of Sb isotopes between the dissolved and solid phases at this particular spot where reducing conditions were observed.

3.4. Antimony mineralogy and speciation as studied at the particle and molecular scales

To study the mineralogy of solid samples in the stormwater ponds, we have performed powder XRD measurements (Fig. SI-1.4). The main mineralogical components (>1%wt) are usual geogenic surface minerals such as quartz, calcite and feldspars. At low diffraction angle, the presence of phyllosilicates such as chlorite, illite and kaolinite is observed on the basis of the (001) reflexions, and small amounts of

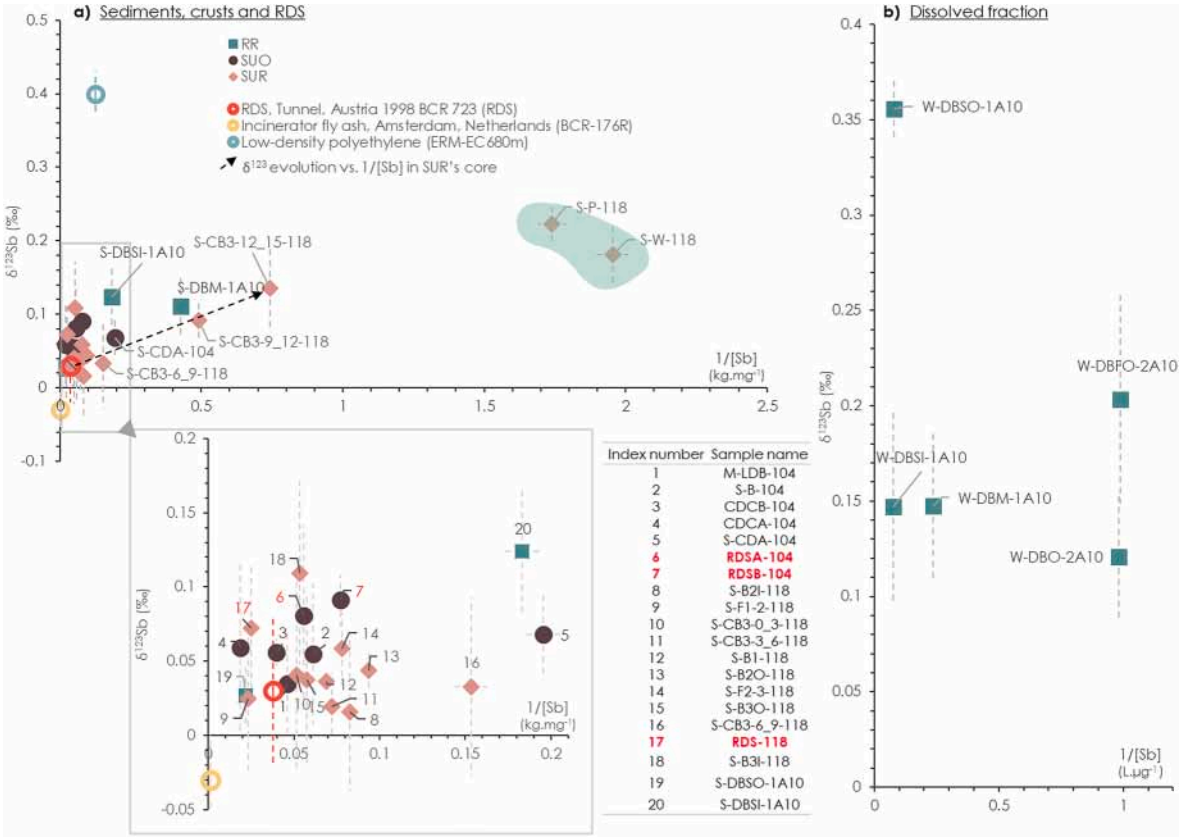

Fig. 3. δ^{123}Sb as a function of 1/[Sb] (Sb concentration in kg.mg^{-1} or L.µg^{-1}) given for (a) sediments, crusts, RDS and (b) water samples (dissolved fraction). Samples from SUR system are represented as pink diamonds; sediments, soils, crusts and RDS from SUO system are represented as dark purple dots; sediments from RR system are represented as blue filled squares. δ^{123}Sb values from certified reference materials published by Ferrari et al., (2021) are also represented: tunnel RDS (BCR 723) in red circle, incinerator fly ash (BCR -176R) in yellow circle and low-density polyethylene (ERM-EC 680 m) in blue circle. The supposed local natural signatures are circled by a light blue area and samples from a core situated along the black dotted arrow. RDS sample labels are represented in red in the zoom figure and in the associated table. δ^{123}Sb data and Sb concentrations are available in Table SI-1.9 in Tables SI-1.3 and SI-1.5, respectively. (For interpretation of the references to colour in this figure legend, the reader is referred to the Web version of this article.)

additional dolomite were observed in the SUR system samples. For some samples, a weak reflexion around 8.4 Å indicates the presence of amphibole-type minerals.

A systematic SEM-EDXS study was carried out on the samples with the objectives of (1) documenting the mineralogy of these Sb-enriched samples constituted of both natural and road derived materials at the aggregate scale, and (2) uncovering discrete Sb-bearing phase(s) (Fig. 4). Depending on the input of local geogenic particles in the samples, mineral aggregates of varying sizes (>2 µm) (Fig. SI-1.5) were observed. In particular, in RDS samples, we observed metallic spherules possibly resulting from abrasion of car/road materials (Fig. SI-1.7). In general, in all samples, particles made of metallic alloys were observed, *e.g.* particles containing Ti, Cr, Cd, Zn and rare earth elements (REE) (Fig. SI-1.6). An important contribution of iron oxyhydroxides/oxides was also observed. Antimony was detected in particles in the three pond systems *via* punctual EDXS analysis using the *L*-emission lines as diagnostic spectral pattern ($L\alpha_1$ 3,604.72 eV, $L\alpha_2$ 3,595.32 eV, $L\beta_1$ 3,843.57 eV, $L\beta_2$ 4,100.78 eV, $L\gamma_1$ 4,347.79 eV and $L\iota$ 3,192 eV). In the RR samples S-DBI-1A10 (Fig. 4a) and S-FBPI-1A10 (Fig. 4b), the analysed Sb-bearing particles showed different chemical compositions depending on the spot where the analysis was performed. Indeed, the presence of Sb is always concomitant with the one of Fe, while Sp1 and Sp6 spots (Fig. 4a) qualitatively show the additional presence of S, Cu and Na. The sample S-FBPI-1A10 (Fig. 4b) shows the presence of Zn and particularly high level of Sb at discrete submicrometric spots, especially in Sp2 where Sb content is qualitatively higher than Fe. In the sample S–F1_2–118 from the SUR system (Fig. 4c), Sb was also found as submicrometric particles associated with Fe oxyhydroxides/oxides. Punctual EDXS spectra (Sp1, Sp2 and Sp3) and EDXS spectra of areas (Sp4 and Sp5) show roughly the same amount of S, Fe and Cu, but Cr and Ba are also detected. Sp2 spectrum, taken on the spot presenting the higher backscattering intensity accordingly shows the highest Sb signal compared to spectra Sp1 and Sp3. In SUO system, on sample CDCB-104 (Fig. 4d), the particle containing Sb was also observed as associated with an iron-containing particle (containing also major elements such as Ca). Because the Ca *K*-emission line overlaps with the main *L*-emission line of Sb, the signal is more difficult to distinguish but remains visible, for instance in the Sp1 spectra (Fig. 4d) in which Cu, S and Ba are also detected.

Calibrated and normalized XANES data include both samples from the field and selected reference compounds (Fig. 5). The reference compounds selected in which Sb is under the Sb(V)–O form are tripuhyite ($FeSbO_4$) and ferrihydrite co-precipitated in the presence of dissolved Sb(V). The reference compounds selected in which Sb is under the Sb(III)–O form are ferrihydrite co-precipitated in the presence of dissolved Sb(III) and Sb_2O_3. Finally, the chosen reference compound representative of the Sb(III)–S molecular environment is amorphous Sb_2S_3. Additionally, the metallic Sb foil was considered as a Sb(0) metal/alloy reference. Qualitative examination of XANES spectra (Fig. 5) shows that the maximum of absorption of the "dry" samples is shifted towards the higher energies, *i.e.* the oxidized species with oxygen ligand Sb(V)–O. On the contrary, the "Underwater" samples show maxima shifted towards lower absorption energies and therefore present a non-negligible contribution of reduced Sb species (*e.g.* Sb(III)–O and/or Sb

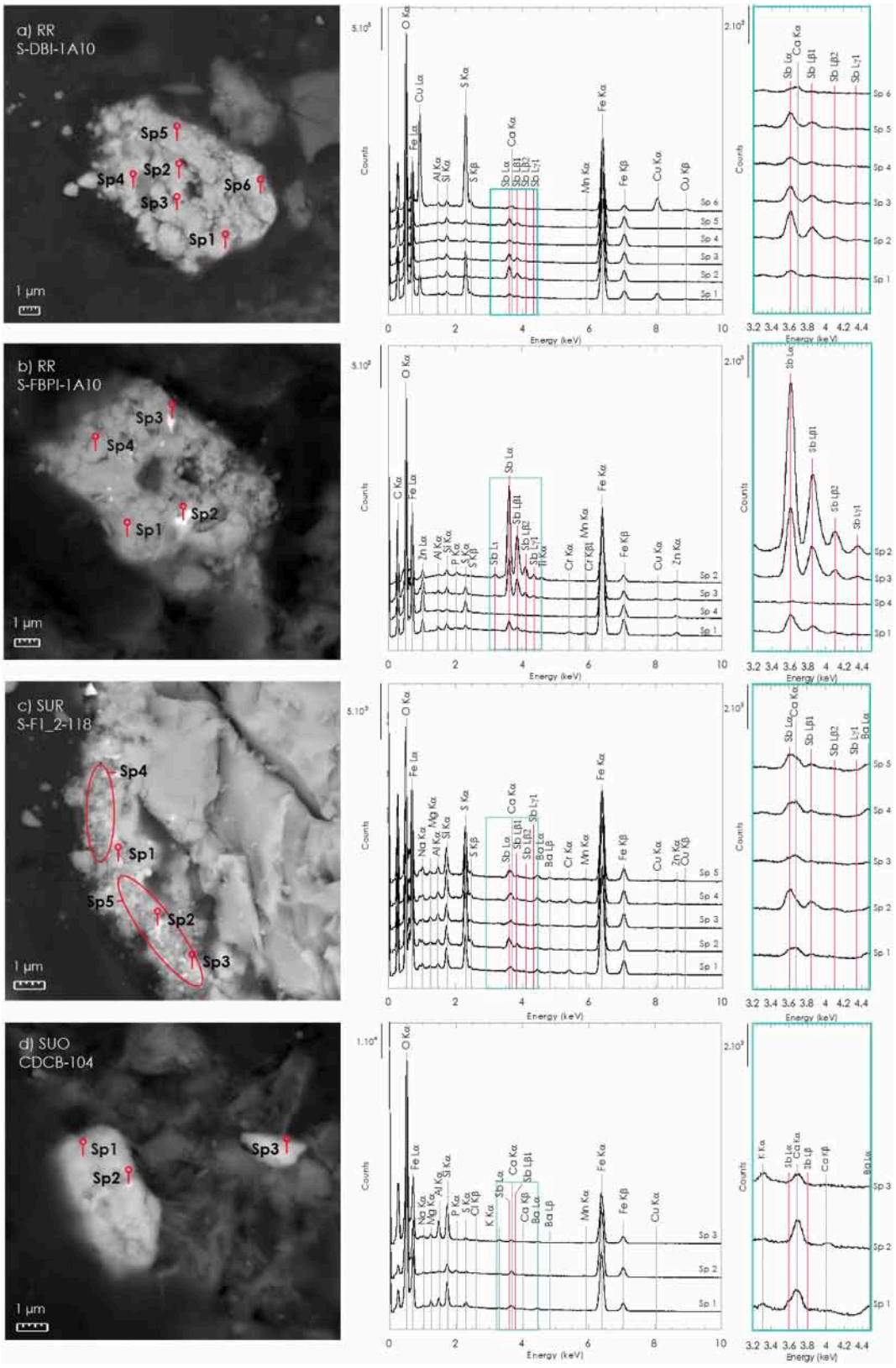

Fig. 4. SEM images taken in backscattering mode (left), and qualitative EDXS analyses (right) for three samples representative of each highway stormwater pond systems SUR, SUO and RR. A zoom between 3.2 and 4.4 KeV on the X-Ray emission spectra (green rectangle) shows the presence of Sb on the basis of the $L\alpha_1$ to $L\iota$ emission lines. (a) underwater sediment S-DBI-1A10 in RR pond system, (b) dry sediment S-FBPI-1A10 in RR pond system, (c) dry sediment S-F1_2-118 in the SUR pond system, (d) dry crust sample CDCB-104 in the SUO pond system. (For interpretation of the references to colour in this figure legend, the reader is referred to the Web version of this article.)

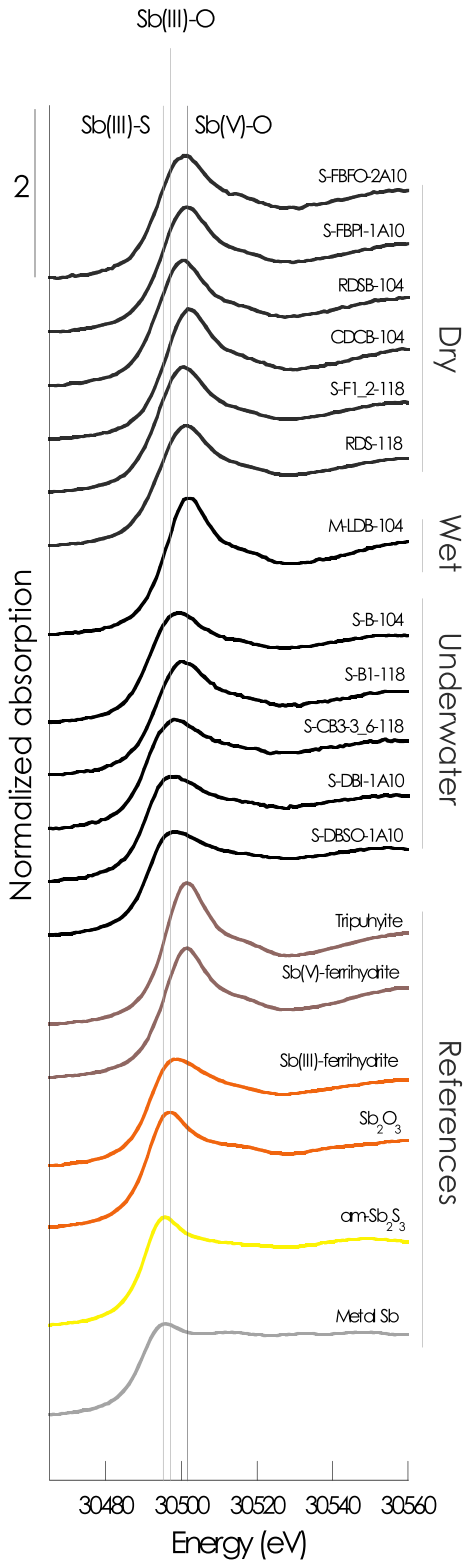

Fig. 5. Antimony *K*-edge XANES spectra of dry and wet samples, underwater samples (black) collected in the three studied sites in the Paris region (France), Sb(V)–O references (brown) are tripuhyite ($FeSbO_4$) and Sb(V) co-precipitated ferrihydrite; Sb(III) references are Sb(III) co-precipitated ferrihydrite, Sb_2O_3 (orange) and amorphous Sb_2S_3 (yellow); Sb(0) is represented by metal Sb (grey). Vertical lines represent the maximum of XANES signal for known chemical environments and ligands, namely Sb(V)–O (30,501 eV), Sb(III)–O (30,497–30,499 eV), Sb(III)–S (30,496 eV), and Sb(0) (Sb–Sb, 30,496 eV). (For interpretation of the references to colour in this figure legend, the reader is referred to the Web version of this article.)

(III)–S).

To quantify the contribution of different oxidation states and ligands in Sb speciation, we proceeded to a LCF analysis on the derivative of the Sb *K*-edge XANES spectra using three reference samples representative of the system geochemistry, namely Sb(V)-ferrihydrite (Sb(V)–O), Sb (III)-ferrihydrite (Sb(III)–O), and amorphous Sb_2S_3 (Sb(III)–S). Results of LCF are presented on Fig. 6 and in Table SI-1.10. In the "dry" samples, the Sb(V)–O form dominates although the Sb(III)–O species are present in significant proportions, between 21% and 48%, except in CDCB-104 in which only the Sb(V)–O form is detected. Likewise, the "wet" sample M-LDB-104 contains only Sb(V)–O species. In contrast, in the "underwater" samples, Sb speciation is dominated by the Sb(III)–S species (from 41% to 80%). Fig. 6c presents Sb speciation normalized to total Sb concentrations in the samples. Thus, we observe that "underwater" samples presenting the main Sb(III)–S signature are likely less concentrated in Sb, between 13.9 mg kg^{-1} for S-CB3-3_6–118 to 45.3 mg kg^{-1} for S-DBSO-1A10 than "dry" samples presenting concentrations up to 93 mg kg^{-1} in the S-FBPI-1A10 sample (Fig. 6c).

4. Discussion

4.1. Geochemical parameters as tracers of emission sources in near-road environments

Radiogenic Pb isotope ratios validate the 2 categories established by the land-use observed in the drained area of the systems: semi-urban (SUO and SUR) and rural systems (RR), on the basis of our knowledge of Pb isotopic endmembers in urban areas. Moreover, heterogeneous isotopic signatures observed and the close to former lead gasoline signatures in 2 samples of the RR system show that Pb isotopes cannot be directly used to infer the age of highway stormwater ponds (see SI-3). Indeed, lead gasoline signature has been shown to still contribute to impact urban environments (Ayrault et al., 2012; Resongles et al., 2021).

Enrichment factors ranging between 0.4 and 130 are observed for Co, Cr, Ni, Cu, Zn, Cd, Sb and Pb. They are of the same magnitude with those previously observed in near road environments (Meland et al., 2010). Different sources for these metals are evoked in the literature, among which abrasion of brake linings for Cu, Sb, Zn, Pb, Cr and, to a lesser extent, of Ni and Cd (Sörme and Lagerkvist, 2002; Hjortenkrans et al., 2007; Thorpe and Harrison, 2008). Zinc, which is strongly enriched in our system, is also used in tires and motorway crash barriers (Sörme and Lagerkvist, 2002; Zhang et al., 2004; Hjortenkrans et al., 2007). Cobalt, Zn, Pb, Cr, Ni and Cd, as constituents of car bodies, can be released to the environment by simple rain leaching (Sörme and Lagerkvist, 2002), probably explaining a part of the emissions given the high flux of vehicles on the road investigated (Table 1). In this study, enrichments in Cd, Cr and Ni are found to be more limited in sediments and SPM in comparison with the data of Hjortenkrans et al. (2007) in road environments. Here, the higher EFs of Pb in semi-urban systems sediments compared to the rural system is in line with the results of Pb isotopic signatures that indicate a major urban source contribution. Cadmium and Cr, presenting higher concentrations in the SUR system compared to RR and SUO systems, (Fig. SI-1.2) might have a different or an additional source at SUR compared to RR and SUO (Fig. 2). Both Cr and Cd enrichments occurred in the third basin (B3, SUR system), also connected to the natural pond (Fig. 1), itself hydrologically connected to the overlying Fontainebleau sand aquifer. We thus hypothesize that Cd and Cr could have been emitted by past industrial/urban activities (Avino et al., 2008; Byrne et al., 2017) on the Plateau of Saclay situated upstream and/or by a geogenic source from the Fontainebleau sands aquifer (which geochemistry is not known at this particular spot). Correlations of Sb with Cu concentrations in the solid phase (Fig. SI-1.2) point to a potential common source such as emission from brake pads (Thorpe and Harrison, 2008). If the ratio Cu/Sb is constant in the road environment, and different from that of the geochemical background, it

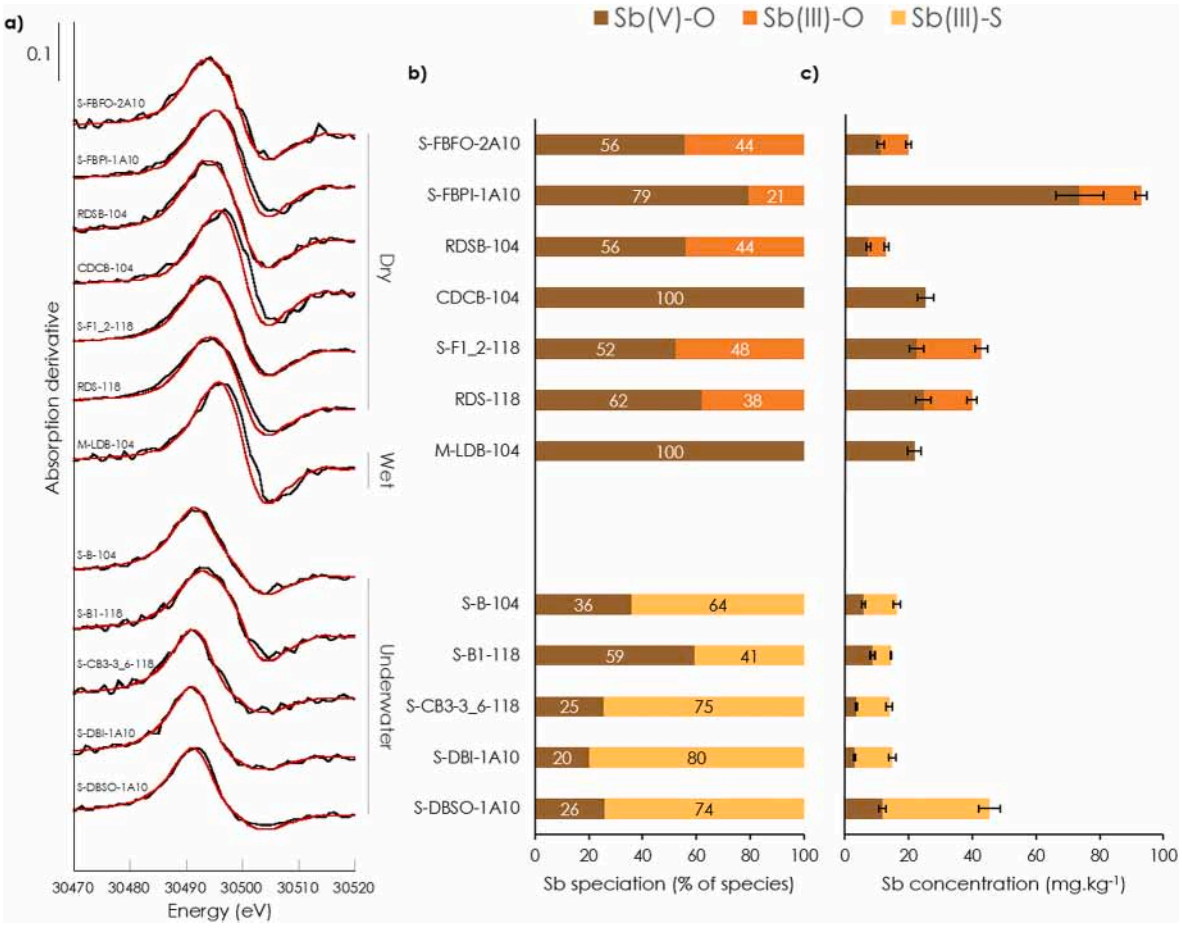

Fig. 6. (a) Results of the linear combination fitting procedure applied on the absorption first derivative of XANES spectra (experimental data in black and fit in red). (b) Proportion of Sb(V)–O species (brown), Sb(III)–O species (orange) and Sb(III)–S species (yellow) normalized to 100% (more details of the species in supplementary information). (c) Results Sb concentrations (mg.kg^{-1}) of each species in the samples. Errors on components determined by LCF are considered to be 10%. (For interpretation of the references to colour in this figure legend, the reader is referred to the Web version of this article.)

is then possible to determine the anthropogenic contribution in the environment studied. Fig. SI-1.8 represents Cu/Sb ratios of the collected solid samples as compared to the Cu/Sb ratios listed in the literature. In the literature, brake pads Cu/Sb is 16.5 on average with variations from 3.5 to 29 (Weckwerth, 2001; Hjortenkrans et al., 2007; Dong et al., 2017). In Sweden, this high range of observed values was explained by the occurrence of different brake suppliers. In the study of Hjortenkrans et al. (2006) focusing on PM_{10}, Cu/Sb are between 4.9 and 15.1 with a median of 5.5. Top soils collected at less than 0.5 m from the road pavement show mean Cu/Sb of 20 (Hjortenkrans et al., 2006) and Cu/Sb ratio of 28 was measured in RDS (Dong et al., 2017). Here, the RDS samples show low Cu/Sb values, ($6 \leq Cu/Sb \leq 7$). Excluding the SUR natural pond ($Cu/Sb \geq 14.8$), the underwater sediments show Cu/Sb values between 5.2 and 10.7, which is well below the values determined for the local geochemical background ($Cu/Sb = 25$). Finally, the important range of variation measured for this geochemical indicator does not validate its use as a specific source tracer in the present study. A possible source of variation could be that Sb and Cu could also be emitted by oil leakages containing anti-frictions materials such as tin-based babbit alloys used as dry lubricants in engine bearings in case of oil pump failure, themselves presenting various compositions (Paleu et al., 2016).

Zinc concentrations in solid samples are positively correlated with Sb concentrations (Fig. SI-1.2, R^2 of 0.92 and 0.73 for RR and SUO respectively, and 0.65 for SUR (0.99 excluding RDS-118)), also pointing to a possible common source in road environments. In the SUR system, the RDS sample (RDS-118) might contain a fraction of galvanized steel issued from the sampled surface, explaining its high Zn concentration. As the Zn–Sb correlation is observed both in urban and rural environments, the source of emission is likely due to abrasion of vehicles constituents, including brake pads (Hjortenkrans et al., 2007).

4.2. *Antimony elemental and isotopic geochemistry and associated sources*

Antimony concentrations in dissolved fractions (0.26–13.2 μg.L^{-1}) are comparable to the concentrations measured in a stormwater pond in Oxford (0.67–8.19 μg.L^{-1}, Kamalakkannan et al., 2004). These values are higher than the ones observed in the Orge River even in the highly urbanized areas (0.23–0.44 μg.L^{-1} at Viry-Châtillon, Le Pape et al., 2012). In the SUR natural pond not impacted by traffic runoff, the high dissolved concentration of Sb (12.5 μg.L^{-1}) does not reflect the concentrations in the corresponding sediment (0.5 mg kg^{-1}) and SPM (6.1 mg kg^{-1}) fractions. Explaining this particular enrichment in dissolved Sb would need further research to determine if it was a punctual anomaly (*e.g.* local contamination of the overlying aquifer) or a permanent input from the Fontainebleau sand aquifer waters. Our values only exceptionally exceed the European guidelines for Sb concentration in drinking water fixed at 10 μg.L^{-1} (directive UE, 2020/2184) and are below the drinking water guidelines for antimony (<20 μg.L^{-1}) as stated by the World Health Organization (Guidelines for Drinking water quality, 2017).

All the solid samples collected in the ponds, including sediments, crusts and soils, present an average δ^{123}Sb signature of 0.07 ± 0.05‰

(n = 25), which is close to the RDS reference material (BCR-723, δ^{123}Sb of 0.03‰, Ferrari et al., 2021). Additionally, the δ^{123}Sb signatures of RDS samples measured in this study (Fig. 3) are also close to the BCR-723 signature. The RDS signature could then reflect a mean isotopic signature of Sb in brake pads in use in France over the last decennials. The low concentrated sediment samples in the SUR natural pond (0.5–0.6 mg kg^{-1}) show heavier δ^{123}Sb signatures (S–W-118 0.18 ± 0.04‰ and S–P-118 0.22 ± 0.03‰) than most of the samples from the stormwater ponds on the same site (Fig. 3). We could thus hypothesize that these samples could trace the local geochemical end-member (Fig. 3, in green), and/or a different source resulting from the industrial activities of the Saclay plateau located above. Nevertheless, the hypothesis of a local Sb contamination source different from the road is less plausible considering the low concentrations and EF measured in the natural pond. Moreover, δ^{123}Sb and the Sb concentrations of the core samples vary slightly from the bottom to the top with a heavier signature δ^{123}Sb =0.13‰ at the bottom (1.3 mg kg^{-1}) going down to 0.04‰ at the top sample with a higher concentration (19 mg kg^{-1}). Considering the local background signature hypothetically determined as 0.18–0.22‰ in the natural pond of the SUR pond system, this variation could be explained by the higher contribution of geogenic materials in deeper samples. Albeit global δ^{123}Sb signature points towards a close range of values, the local variation observed on some samples could putatively be ascribed to fractionation due to post-depositional processes. Indeed, in the RR-2A10 pond, two samples present diverging δ^{123}Sb values in the dissolved fraction (W-DBFO-2A10 and W-DBO-2A10) while having the same Sb concentration. DBFO could represent the δ^{123}Sb value for input water whereas DBO could represent the equilibrated value after a longer residence time in the pond. This might be due to isotope fractionation between the dissolved and solid fractions in the pond due to specific biogeochemical processes (reduction/oxidation/ligand exchange) occurring within the sediments, potentially attesting of Sb exchanges between the solid phase and the overlying water column. In the RR-1A10 reed-planted pond, particularly interesting observations are made for the samples DBSI, DBM, and DBSO, located from the entrance to the exit of the settling pond, respectively. For DBSI and DBM, dissolved and sediment fractions present similar δ^{123}Sb signatures (DBSI, 0.15 ± 0.05‰ dissolved *vs.* 0.12 ± 0.04‰ solid, and DBM, 0.15 ± 0.04‰ dissolved *vs.* 0.11 ± 0.04‰ solid) whereas for DBSO they significantly differ (0.36 ± 0.02‰ dissolved *vs.* 0.03 ± 0.02‰ solid). We could hypothesize that this particular fractionation at the DBSO site could possibly be a consequence of Sb(V) reduction to Sb(III) under anoxic conditions, and/or to ligand exchange from oxygen to sulphur (Rouxel et al., 2003; Ferrari et al., 2022), which would be supported by the LCF-XANES analysis on this Sb-rich (45.3 ± 2.7 mg kg^{-1}) sample showing an important contribution of reduced Sb (Sb(III)–S = 74 ± 10% *vs.* Sb(V)–O = 26 ± 10%). A smell of sulphide was also noticed at the DBSO sampling point, indicative of sulphide-producing conditions that might also induce a fractionation of Sb between dissolved and solid fractions, for instance due to production of thio-Sb intermediates (Ye et al., 2019). Alternatively, other physico-chemical processes could play a role in Sb isotope fractionation. For instance, preferential adsorption of light Sb isotope has been observed with Sb(V) on alumina due to kinetic effects, leaving heavier Sb isotope in aqueous phase (Zhou et al., 2022).

SEM-EDXS allowed us to observe discrete phases carrying Sb (Fig. 4) directly pointing to the brake pad source. In the three systems, Sb was similarly observed on micro-particles with high backscattering signal associated to iron oxides (Fig. 4). In these particles, Fe, S, Cu, Zn and Ba are observed in addition to Sb (Fig. 4), as it has already been observed in some brake pads (Ingo et al., 2004). Due to brake friction, the high temperature leads to the oxidation of Sb_2S_3 lubricant and oxidizes Sb_2S_3 into Sb_2O_5, Sb_2O_3 and/or Sb_2O_4, depending on the temperature generated by the braking process and the initial composition of brake pads (Ingo et al., 2004; Cho et al., 2006; Martinez and Echeberria, 2016). These Sb oxides would then react with metallic iron included in the brake pad to form iron oxides, metallic Sb, and/or Fe–Sb containing alloys (Matějka et al., 2011; Martinez and Echeberria, 2016). Even if its use will probably tend to decrease since health and environment safety decisions in the USA are leading to a ban of Sb in brake pads (US EPA Copper-Free Brake Initiative), these observations and the nature of phases containing Sb observed by SEM-EDXS strongly suggest that brake pads are a present-day source of Sb emission from road traffic at the sampling sites. It is important to note that Sb could also be present, even in a large extent, as associated with mineral phases at lower concentration, non-detectable with the SEM-EDXS method.

4.3. Antimony geochemical reactivity in road impacted surface environments

Linear combination fits of XANES derivative spectra at the Sb *K*-edge show that both Sb(V)–O and Sb(III)–O are observed in solids sampled in "dry" oxic conditions (Fig. 5). In a previous study, Sb(III) and Sb(V) with both oxygen and sulphur ligands have been detected in urban road samples such as RDS and aerosols (10 μm and 2.5 μm) (Varrica et al., 2013). In this latter study, the authors interpret their speciation as a result of Sb_2S_3-containing brake pad abrasion producing Sb oxides (Sb_2O_3 (Sb(III)–O), and Sb_2O_5 (Sb(V)–O) species) as also identified by Matějka et al. (2011). Here, we confirm that, in dust directly produced by road traffic, *i.e.* in the RDS sampled upstream from the studied pond systems, mixed Sb(V)–O/Sb(III)–O oxidation states were present, which would also be in agreement with emissions from brake pads. This tends to indicate, together with SEM-EDXS observations previously discussed, that this source is still active, from direct brake pad abrasion, or from leaching of ancient asphalt surfaces (Dong et al., 2017; Spreadbury et al., 2021).

Antimony speciation is driven by both biotic and abiotic geochemical processes including direct Sb bacterial respiration (Li et al., 2016; Loni et al., 2019) and secondary Sb reduction by reductants produced by bacterial respiration. For instance, antimony(V) reduction can be caused by local production of electron donors such as Fe(II) or sulphides, themselves biogenically produced in anoxic/suboxic conditions by Fe (III)-reducing or sulphide producing bacteria. For instance, bio-reduction of Fe(III)-oxyhydroxides induces a release of Fe(II) into the water and a precipitation of secondary Fe(III) bearing minerals (Burton et al., 2019, 2020). This precipitation may cause the incorporation of Sb (V) species in the neoformed minerals *via* Fe(III) substitution (Hockmann et al., 2021) or Sb(V) reduction to Sb(III) (Kirsch et al., 2008). Sb (V) reduction can also be mediated by reduced organic matter such as humic acids when associated to Fe(II) in solution (Karimian et al., 2019). In turn, sulphide produced by bacteria can result in Fe (III)-oxyhydroxides sulphidation followed by the release of Sb(III) and the subsequent formation of soluble Sb(III)–S species (Ye et al., 2019; Hockmann et al., 2020; Ye and Jing, 2022). Finally, abiotic processes resulting from surface electrons transfer from Fe and Mn oxyhydroxides to Sb(III) species under oxic atmosphere have been shown to occur at both acidic and neutral pH, resulting in Sb(III) oxidation (Belzile et al., 2001).

No direct speciation data are currently available on Sb emitted from road dust contamination when transferred to surrounding surface environments such as soils, sediments and hydrosystems. In the studied pond systems, representative of surface accumulator media, two distinct patterns were discernible. Indeed, solids sampled in oxic "dry" conditions present exclusively oxygen-bound form of Sb, while an additional sulphur-bound form is observed for suboxic underwater samples. This observation would support the hypothesis of local biogeochemical transformations. This is in line with the results of Arsic et al. (2018) who observed a significant contribution of Sb(III)–S species (25%–60%) in their experiments of anoxic sediment incubation under a water column and with Ye and Jing (2022) showing the immobilisation of Sb in the Sb_2S_3 form due to S(0) reduction by *Shewanella oneidensis* MR-1 in the presence of Sb(III) adsorbed goethite. Here, we observe an important contribution of Sb(III)–S (41% - 80%) in the underwater samples even if

we cannot exclude the minor presence of Sb(III)-O species given the uncertainty of the LCF-XANES method. Since Sb_2S_3 is constitutive of brake pads, we cannot exclude that a part of the measured Sb(III)–S contribution could originate directly from Sb_2S_3 fragments even if its oxidation is mainly expected due to brake friction (Matějka et al., 2011; Martinez and Echeberria, 2016). If produced by local biogeochemical reactions as shown in the study of Arsic et al. (2018), in the present study, questions remain on the actual identity of the Sb(III)–S phases present in our samples. Indeed, such a Sb(III)–S XANES spectral contribution could be the signature of Sb bonding to thiol functional groups of organic matter (OM) (Besold et al., 2019a, 2019b) or Sb(III) association with iron sulphide such as FeS or FeS_2 (Kirsch et al., 2008; Hockmann et al., 2020), or of amorphous Sb-sulphide as observed elsewhere (Kulp et al., 2014; Bennett et al., 2017; Besold et al., 2019a, 2019b; Ye and Jing, 2022).

Thioantimonate species have been designated as potential intermediates of these sulphidation reactions, having particular consequences on Sb mobility for instance by limiting Sb affinity to iron oxides (Ye et al., 2019, 2021). The presence of minor amounts of such thio-Sb forms, including within the solid phase, could not be excluded since XANES spectra of sorbed thio-Sb at the Sb *K*-edge should contribute in between the Sb–O and Sb–S species. In the literature, the sulphidation process of particles such as Sb(V)-containing oxyhydroxides has recently been reported to result in an important Sb mobilization towards the aqueous phase, likely resulting in Sb depletion in the solid fraction (Hockmann et al., 2020). Here, Sb concentrations were on average lower in underwater samples compared to the ones sampled on surfaces exposed to air, which would be in line with this process. Alternatively, this difference of concentration could be due to dilution of Sb inputs by detrital particles accumulating in the basins.

In underwater samples of the present study, no statistically significant contribution from Sb(III)–O species were detected on the basis of the evolution of the reduced chi-square when adding a fitting component. In contrast, Arsic et al. (2018)'s study has observed this species even under anoxic conditions, and Besold et al. (2019a) also observed an important Sb(III)–O contribution in peatland samples. In this latter study, the authors conclude that the high organic content and/or the particular nature of OM would stabilize the Sb(III)–O form, which could also be the case for Arsic et al. (2018). In their study focusing on Fe oxyhydroxides sulphidation experiments, Hockmann et al. (2020) only observed a weak contribution of the Sb(III)–O species in the solids, in particular in their low sulphidic system, which could be related to the fact that only a negligible fraction of insoluble antimonite is detected in the aqueous phase.

In the underwater sample S-DBSO-1A10, situated upstream in the RR pond system, the major species are Sb(III)–S ($74 \pm 10\%$) with only $26 \pm 10\%$ of Sb(V)–O, while in the dry sample S-FBPI-1A10, located very close on the same hydrologic pathway but at the open air, our results show 79% of Sb(V)–O and 21% of Sb(III)–O. This means that over a short spatial course, Sb shows significant differences in its redox geochemistry. Thus, this would confirm that Sb speciation is particularly versatile in such surface environments, likely driven by the local redox potential. Indeed, changes from anoxic to oxic media result in dramatic changes of Sb oxidation state and coordination chemistry. In addition, the fact that dry samples are more concentrated in Sb than underwater samples would likely support the hypothesis of a Sb transfer, for instance in the dissolved phase, and potentially resulting from release due to Sb sulphidation upstream in the pond as evoked previously. These results raise questions about the mobility properties of Sb at the liquid/solid interface in stormwater ponds, in particular because water fluctuations often occur in these ponds, due to evaporation associated with long dry periods, and storm events or management operations.

5. Conclusion

This study brings new information about antimony isotope geochemistry and speciation in stormwater pond accumulator media representative of surface environments impacted by road runoff such as urban areas. Both semi-urban and rural ponds are observed to be contaminated with a cocktail of inorganic contaminants clearly identified as emitted by road traffic (Cu, Zn, Sb and Pb). Additional inorganic contaminants (Cd, Ni and Cr) are particularly observed in urban ponds and their presence is interpreted to originate from anthropogenic urban/industrial activities. The Pb isotope ratio dataset shows that the impact of urban areas is significant even if the sampling sites are not directly connected to urban networks, which would reflect a contamination at a larger scale, likely due to atmospheric particle inputs or to urban particles reemitted by leaching of vehicles during rain events. Antimony is the most enriched element in both rural and urban highway stormwater ponds exposed to the road traffic source. For the first time, Sb isotope composition ($\delta^{123}Sb$) of solids in the road to pond continuum is measured and shows a homogenous value among the different road-impacted sites, giving access to the mean signature of the Sb-containing brake lining materials used in France during last decades. Preliminary data obtained on both solid and dissolved phases at the rural site indicate that $\delta^{123}Sb$ use as (bio)geochemical tracer is promising and should be further studied. Then, we show that Sb is subjected to important changes of speciation (oxidation state and ligands) in the road-to-pond waterway, and is thus highly sensitive to redox changes at the stormwater pond scale. To this respect, a perspective of research is to study the geochemical reactivity of Sb upon aging when the contaminated stormwater pond sediments are submitted to long period of dryness. Thus, mobility of Sb from the main Sb-bearing phases observed should be evaluated to help to manage this contamination. From the results presented here, we posit that the processes leading to speciation and isotopic modifications should be studied in details for a better management of Sb contamination in stormwater pond infrastructures and downstream aquatic environments, and subsequently in urban surface environments exposed to road traffic contaminations.

Credit author statement

Maëva Philippe: Conceptualization, Methodology, Investigation, Formal analysis, Writing - Original Draft, Writing - Review & Editing - **Pierre Le Pape**: Conceptualization, Methodology, Investigation, Formal analysis, Writing - Original Draft, Writing - Review & Editing, Supervision - **Éléonore Resongles**: Investigation, Formal analysis, Writing - Review & Editing - **Gautier Landrot**: Investigation, Software, Writing - Review & Editing - **Rémi Freydier**: Investigation, Formal analysis - **Ludovic Delbes**: Investigation - **Louise Bordier**: Investigation, Formal analysis, Writing - Review & Editing - **Benoît Baptiste**: Software, Investigation - **Camille Baya**: Investigation - **Corinne Casiot**: Methodology, Writing - Review & Editing - **Sophie Ayrault**: Conceptualization, Methodology, Investigation, Formal analysis, Writing - Original Draft, Writing - Review & Editing, Project administration, Supervision.

Declaration of competing interest

The authors declare that they have no known competing financial interests or personal relationships that could have appeared to influence the work reported in this paper.

Data availability

Data will be made available on request.

Acknowledgments

We thank the SOLEIL Synchrotron for having provided beamtime. We are grateful to Erik Elkaïm for his help during XRD measurements of ferrihydrite reference compounds used in this study at the CRISTAL beamline (BAG proposal 20201440) and to SAMBA beamline staff help during XANES measurements. We thank the IMPMC SEM-FIB plateform staff (Imène Estève, Béatrice Doisneau, Stéphanie Delbrel), the DiRIF service and COFIROUTE company for granting us access to their installations and for sharing information about their management. We thank Manon Stope for her help during the preparation of samples prior to Sb isotope analysis and Colin Ferrari and Sophie Delpoux for their help during Sb analysis at the AETE-ISO platform, (OSU-OREME/Université de Montpellier). This work was financially supported by the CNRS INSU-INEE EC2CO program and the PIREN-Seine Program. This work has been conducted in the framework of the PhD thesis of Maëva Philippe at Paris-Saclay University (ED 579 SMEMaG).

Appendix A. Supplementary data

Supplementary data to this article can be found online at https://doi.org/10.1016/j.chemosphere.2022.137368.

References

Ahmed, F., Ishiga, H., 2006. Trace metal concentrations in street dusts of Dhaka city, Bangladesh. Atmos. Environ. 40, 3835–3844.
Amereih, S., Meisel, T., Scholger, R., Wegscheider, W., 2005. Antimony speciation in soil samples along two Austrian motorways by HPLC-ID-ICP-MS. J. Environ. Monit. 7, 1200–1206.
Arsic, M., Teasdale, P.R., Welsh, D.T., Johnston, S.G., Burton, E.D., Hockmann, K., Bennett, W.W., 2018. Diffusive gradients in thin films reveals differences in antimony and arsenic mobility in a contaminated wetland sediment during an oxic-anoxic transition. Environ. Sci. Technol. 52, 1118–1127.
Avino, P., Capannesi, G., Rosada, A., 2008. Heavy metal determination in atmospheric particulate matter by Instrumental Neutron Activation Analysis. Microchem. J. 88, 97–106.
Ayrault, S., Roy-Barman, M., Le Cloarec, M.-F., Priadi, C.R., Bonté, P., Göpel, C., 2012. Lead contamination of the Seine River, France: geochemical implications of a historical perspective. Chemosphere 87, 902–910.
Belzile, N., Chen, Y.-W., Wang, Z., 2001. Oxidation of antimony (III) by amorphous iron and manganese oxyhydroxides. Chem. Geol. 174, 379–387.
Bennett, W.W., Hockmann, K., Johnston, S.G., Burton, E.D., 2017. Synchrotron X-ray absorption spectroscopy reveals antimony sequestration by reduced sulphur in a freshwater wetland sediment. Environ. Chem. 14, 345–349.
Besold, J., Eberle, A., Noël, V., Kujala, K., Kumar, N., Scheinost, A.C., Pacheco, J.L., Fendorf, S., Planer-Friedrich, B., 2019a. Antimonite binding to natural organic matter: spectroscopic evidence from a mine water impacted peatland. Environ. Sci. Technol. 53, 10792–10802.
Besold, J., Kumar, N., Scheinost, A.C., Lezama Pacheco, J., Fendorf, S., Planer-Friedrich, B., 2019b. Antimonite complexation with thiol and carboxyl/phenol groups of peat organic matter. Environ. Sci. Technol. 53, 5005–5015.
Burton, E.D., Hockmann, K., Karimian, N., Johnston, S.G., 2019. Antimony mobility in reducing environments: the effect of microbial iron(III)-reduction and associated secondary mineralization. Geochem. Cosmochim. Acta 245, 278–289.
Burton, E.D., Hockmann, K., Karimian, N., 2020. Antimony sorption to goethite: effects of Fe(II)-Catalyzed recrystallization. ACS Earth Space Chem 4, 476–487.
Byrne, P., Taylor, K.G., Hudson-Edwards, K.A., Barrett, J.E.S., 2017. Speciation and potential long-term behaviour of chromium in urban sediment particulates. J. Soils Sediments 17, 2666–2676.
Chan, D., Stachowiak, G.W., 2004. Review of automotive brake friction materials. Proc. Inst. Mech. Eng. - Part D J. Automob. Eng. 218, 953–966.
Chen, J., Tan, M., Li, Yulan, Zheng, J., Zhang, Y., Shan, Z., Zhang, G., Yan, Li, 2008. Characteristics of trace elements and lead isotope ratios in PM2.5 from four sites in Shanghai. J. Hazard Mater. 156, 36–43.
Cho, M.H., Ju, J., Kim, S.J., Jang, H., 2006. Tribological properties of solid lubricants (graphite, Sb2S3, MoS2) for automotive brake friction materials. Wear 260, 855–860.
Clozel, B., Ruban, V., Durand, C., Conil, P., 2006. Origin and mobility of heavy metals in contaminated sediments from retention and infiltration ponds. Appl. Geochem. 21, 1781–1798.
Davis, A.P., Shokouhian, M., Ni, S., 2001. Loading estimates of lead, copper, cadmium, and zinc in urban runoff from specific sources. Chemosphere 44, 997–1009.
Degryse, P., Lobo, L., Shortland, A., Vanhaecke, F., Blomme, A., Painter, J., Gimeno, D., Eremin, K., Greene, J., Kirk, S., Walton, M., 2015. Isotopic investigation into the raw materials of Late Bronze Age glass making. J. Archaeol. Sci. 62, 153–160.
Dillis, S., Ham-Meert, A.V., Leeming, P., Shortland, A., Gobejishvili, G., Abramishvili, M., Degryse, P., 2019. Antimony as a raw material in ancient metal and glass making: provenancing Georgian LBA metallic Sb by isotope analysis. Star: Sci. Technol. Archaeol. Res. 1–15.
Dong, S., Ochoa Gonzalez, R., Harrison, R.M., Green, D., North, R., Fowler, G., Weiss, D., 2017. Isotopic signatures suggest important contributions from recycled gasoline, road dust and non-exhaust traffic sources for copper, zinc and lead in PM_{10} in London, United Kingdom. Atmos. Environ. 165, 88–98.
Emmanuel, S., Erel, Y., 2002. Implications from concentrations and isotopic data for Pb partitioning processes in soils. Geochem. Cosmochim. Acta 66, 2517–2527.
Farmer, J.G., Eades, L.J., Atkins, H., Chamberlain, D.F., 2002. Historical trends in the lead isotopic composition of archival sphagnum mosses from scotland (1838−2000). Environ. Sci. Technol. 36, 152–157.
Ferrari, C., Méheut, M., Resongles, E., Freydier, R., Casiot, C., 2022. Equilibrium mass-dependent isotope fractionation of antimony between stibnite and Sb secondary minerals: a first-principles study. Chem. Geol. 611, 121115.
Ferrari, C., Resongles, E., Freydier, R., Casiot, C., 2021. A single-step purification method for the precise determination of the antimony isotopic composition of environmental, geological and biological samples by HG-MC-ICP-MS. J. Anal. At. Spectrom. 36, 776–785.
Filella, M., Williams, P.A., Belzile, N., 2009. Antimony in the environment: knowns and unknowns. Environ. Chem. 6, 95.
Froger, C., Ayrault, S., Evrard, O., Monvoisin, G., Bordier, L., Lefèvre, I., Quantin, C., 2018. Tracing the sources of suspended sediment and particle-bound trace metal elements in an urban catchment coupling elemental and isotopic geochemistry, and fallout radionuclides. Environ. Sci. Pollut. Res. 25, 28667–28681.
Froger, C., Quantin, C., Gasperi, J., Caupos, E., Monvoisin, G., Evrard, O., Ayrault, S., 2019. Impact of urban pressure on the spatial and temporal dynamics of PAH fluxes in an urban tributary of the Seine River (France). Chemosphere 219, 1002–1013.
Gonzalez, R.O., Strekopytov, S., Amato, F., Querol, X., Reche, C., Weiss, D., 2016. New insights from zinc and copper isotopic compositions into the sources of atmospheric particulate matter from two major European cities. Environ. Sci. Technol. 50, 9816–9824.
Hares, R.J., Ward, N.I., 1999. Comparison of the heavy metal content of motorway stormwater following discharge into wet biofiltration and dry detention ponds along the London Orbital (M25) motorway. Sci. Total Environ. 235, 169–178.
Haus, N., Zimmermann, S., Wiegand, J., Sures, B., 2007. Occurrence of platinum and additional traffic related heavy metals in sediments and biota. Chemosphere 66, 619–629.
Helmreich, B., Hilliges, R., Schriewer, A., Horn, H., 2010. Runoff pollutants of a highly trafficked urban road – correlation analysis and seasonal influences. Chemosphere 80, 991–997.
Hjortenkrans, D., Bergbäck, B., Häggerud, A., 2006. New metal emission patterns in road traffic environments. Environ. Monit. Assess. 117, 85–98.
Hjortenkrans, D.S.T., Bergbäck, B.G., Häggerud, A.V., 2007. Metal emissions from brake linings and tires: case studies of stockholm, Sweden 1995/1998 and 2005. Environ. Sci. Technol. 41, 5224–5230.
Hockmann, K., Karimian, N., Schlagenhauff, S., Planer-Friedrich, B., Burton, E.D., 2021. Impact of antimony(V) on iron(II)-Catalyzed ferrihydrite transformation pathways: a novel mineral switch for feroxyhyte formation. Environ. Sci. Technol. 55, 4954–4963.
Hockmann, K., Planer-Friedrich, B., Johnston, S.G., Peiffer, S., Burton, E.D., 2020. Antimony mobility in sulfidic systems: coupling with sulfide-induced iron oxide transformations. Geochem. Cosmochim. Acta 282, 276–296.
Hwang, H.-M., Fiala, M.J., Park, D., Wade, T.L., 2016. Review of pollutants in urban road dust and stormwater runoff: part 1. Heavy metals released from vehicles. Int. J. Urban Sci. 20, 334–360.
Ingo, G.M., D'Uffizi, M., Falso, G., Bultrini, G., Padeletti, G., 2004. Thermal and microchemical investigation of automotive brake pad wear residues. Thermochim. Acta 418, 61–68.
Johansson, C., Norman, M., Burman, L., 2009. Road traffic emission factors for heavy metals. Atmos. Environ. 43, 4681–4688.
Johnston, S.G., Bennett, W.W., Doriean, N., Hockmann, K., Karimian, N., Burton, E.D., 2020. Antimony and arsenic speciation, redox-cycling and contrasting mobility in a mining-impacted river system. Sci. Total Environ. 710, 136354.
Kamalakkannan, R., Zettel, V., Goubatchev, A., Stead-Dexter, K., Ward, N.I., 2004. Chemical (polycyclic aromatic hydrocarbon and heavy metal) levels in contaminated stormwater and sediments from a motorway dry detention pond drainage system. J. Environ. Monit. 6, 175–181.
Karimian, N., Burton, E.D., Johnston, S.G., Hockmann, K., Choppala, G., 2019. Humic acid impacts antimony partitioning and speciation during iron(II)-induced ferrihydrite transformation. Sci. Total Environ. 683, 399–410.
Kibblewhite, M.G., 2018. Contamination of agricultural soil by urban and peri-urban highways: an overlooked priority? Environ. Pollut. 242, 1331–1336.
Kirsch, R., Scheinost, A.C., Rossberg, A., Banerjee, D., Charlet, L., 2008. Reduction of antimony by nano-particulate magnetite and mackinawite. Miner. Mag. 72, 185–189.
Komárek, M., Ettler, V., Chrastný, V., Mihaljevič, M., 2008. Lead isotopes in environmental sciences: a review. Environ. Int. 34, 562–577.
Krachler, M., Zheng, J., Koerner, R., Zdanowicz, C., Fisher, D., Shotyk, W., 2005. Increasing atmospheric antimony contamination in the northern hemisphere: snow and ice evidence from Devon Island, Arctic Canada. J. Environ. Monit. 7, 1169–1176.
Kulp, T.R., Miller, L.G., Braiotta, F., Webb, S.M., Kocar, B.D., Blum, J.S., Oremland, R.S., 2014. Microbiological reduction of Sb(V) in anoxic freshwater sediments. Environ. Sci. Technol. 48, 218–226.
Landrot, G., 2018. FASTOSH: a software to process XAFS data for geochemical & environmental applications. In: Goldschmidt, p. 1402. Boston.

Le Pape, P., Blanchard, M., Brest, J., Boulliard, J.-C., Ikogou, M., Stetten, L., Wang, S., Landrot, G., Morin, G., 2017. Arsenic incorporation in pyrite at ambient temperature at both tetrahedral S–I and octahedral FeII sites: evidence from EXAFS–DFT analysis. Environ. Sci. Technol. 51, 150–158.
Le Pape, P., Ayrault, S., Michelot, J.-L., Monvoisin, G., Noret, A., Quantin, C., 2013. Building an isotopic hydrogeochemical indicator of anthropogenic pressure on urban rivers. Chem. Geol. 344, 63–72.
Le Pape, P., Ayrault, S., Quantin, C., 2012. Trace element behavior and partition versus urbanization gradient in an urban river (Orge River, France). J. Hydrol. 472–473, 99–110.
Lee, W.K., Rhee, T.H., Kim, H.S., Jang, H., 2013. Effects of antimony trisulfide (Sb2S3) on sliding friction of automotive brake friction materials. Met. Mater. Int. 19, 1101–1107.
Li, J., Wang, Q., Oremland, R.S., Kulp, T.R., Rensing, C., Wang, G., 2016. Microbial antimony biogeochemistry: enzymes, regulation, and related metabolic pathways. Appl. Environ. Microbiol. 82, 5482–5495.
Liu, K., Hou, S., Wu, S., Zhang, W., Zou, X., Yu, J., Song, J., Sun, X., Huang, R., Pang, H., Wang, J., 2021. Assessment of heavy metal contamination in the atmospheric deposition during 1950–2016 A.D. from a snow pit at Dome A, East Antarctica. Environ. Pollut. 268, 115848.
Lobo, L., Degryse, P., Shortland, A., Eremin, K., Vanhaecke, F., 2013. Copper and antimony isotopic analysis via multi-collector ICP-mass spectrometry for provenancing ancient glass. J. Anal. At. Spectrom. 29, 58–64.
Loni, P.C., Wu, M., Wang, W., Wang, H., Ma, L., Liu, C., Song, Y., H Tuovinen, O., 2019. Mechanism of microbial dissolution and oxidation of antimony in stibnite under ambient conditions. J. Hazard Mater., 121561
Martinez, A.M., Echeberria, J., 2016. Towards a better understanding of the reaction between metal powders and the solid lubricant Sb2S3 in a low-metallic brake pad at high temperature. Wear 348–349, 27–42.
Matějka, V., Lu, Y., Matějková, P., Smetana, B., Kukutschová, J., Vaculík, M., Tomášek, V., Zlá, S., Fan, Y., 2011. Possible stibnite transformation at the friction surface of the semi-metallic friction composites designed for car brake linings. Appl. Surf. Sci. 258, 1862–1868.
Meland, S., Borgstrøm, R., Heier, L.S., Rosseland, B.O., Lindholm, O., Salbu, B., 2010. Chemical and ecological effects of contaminated tunnel wash water runoff to a small Norwegian stream. Sci. Total Environ. 408, 4107–4117.
Monna, F., Lancelot, J., Croudace, I.W., Cundy, A.B., Lewis, J.T., 1997. Pb isotopic composition of airborne particulate material from France and the southern United Kingdom: implications for Pb pollution sources in urban areas. Environ. Sci. Technol. 31, 2277–2286.
Moriwaki, H., Kitajima, S., Katahira, K., 2009. Waste on the roadside, 'poi-sute' waste: its distribution and elution potential of pollutants into environment. Waste Manag. 29, 1192–1197.
Napier, F., D'Arcy, B., Jefferies, C., 2008. A review of vehicle related metals and polycyclic aromatic hydrocarbons in the UK environment. Desalination 226, 143–150.
Nielsen, K., Kalmykova, Y., Strömvall, A.-M., Baun, A., Eriksson, E., 2015. Particle phase distribution of polycyclic aromatic hydrocarbons in stormwater — using humic acid and iron nano-sized colloids as test particles. Sci. Total Environ. 532, 103–111.
Nory, R.M., Figueiredo, A.M.G., Souto-Oliveira, C.E., Babinski, M., 2021. Urban contamination sources in tunnel dusts from São Paulo city: elemental and isotopic characterization. Atmos. Environ. 254, 118188.
Paleu, V., Georgescu, S., Baciu, C., Istrate, B., Baciu, E.R., 2016. Preliminary experimental research on friction characteristics of a thick gravitational casted babbit layer on steel substrate. In: IOP Conf. Ser.: Mater. Sci. Eng, vol. 147, 012028.
Perron, M.A.C., Pick, F.R., 2020. Water quality effects on dragonfly and damselfly nymph communities: a comparison of urban and natural ponds. Environ. Pollut. 263, 114472.
Priadi, C., Bourgeault, A., Ayrault, S., Gourlay-Francé, C., Tusseau-Vuillemin, M.-H., Bonté, P., Mouchel, J.-M., 2011. Spatio-temporal variability of solid, total dissolved and labile metal: passive vs. discrete sampling evaluation in river metal monitoring. J. Environ. Monit. 13, 1470–1479.
Quiroz, W., Cortés, M., Astudillo, F., Bravo, M., Cereceda, F., Vidal, V., Lobos, M.G., 2013. Antimony speciation in road dust and urban particulate matter in Valparaiso, Chile: analytical and environmental considerations. Microchem. J. 110, 266–272.
Resongles, E., Casiot, C., Freydier, R., Le Gall, M., Elbaz-Poulichet, F., 2015a. Variation of dissolved and particulate metal(loid) (As, Cd, Pb, Sb, Tl, Zn) concentrations under varying discharge during a Mediterranean flood in a former mining watershed, the Gardon River (France). J. Geochem. Explor. 158, 132–142.
Resongles, E., Dietze, V., Green, D.C., Harrison, R.M., Ochoa-Gonzalez, R., Tremper, A. H., Weiss, D.J., 2021. Strong evidence for the continued contribution of lead deposited during the 20th century to the atmospheric environment in London of today. Proc. Natl. Acad. Sci. USA 118, e2102791118.
Resongles, E., Freydier, R., Casiot, C., Viers, J., Chmeleff, J., Elbaz-Poulichet, F., 2015b. Antimony isotopic composition in river waters affected by ancient mining activity. Talanta 144, 851–861.
Rouxel, O., Ludden, J., Fouquet, Y., 2003. Antimony isotope variations in natural systems and implications for their use as geochemical tracers. Chem. Geol. 200, 25–40.
Salma, I., Maenhaut, W., 2006. Changes in elemental composition and mass of atmospheric aerosol pollution between 1996 and 2002 in a Central European city. Environ. Pollut. 143, 479–488.
Sánchez-Rodas, D., Alsioufi, L., Sánchez de la Campa, A.M., González-Castanedo, Y., 2017. Antimony speciation as geochemical tracer for anthropogenic emissions of atmospheric particulate matter. J. Hazard Mater. 324, 213–220.
Sörme, L., Lagerkvist, R., 2002. Sources of heavy metals in urban wastewater in Stockholm. Sci. Total Environ. 298, 131–145.
Spreadbury, C.J., Clavier, K.A., Lin, A.M., Townsend, T.G., 2021. A critical analysis of leaching and environmental risk assessment for reclaimed asphalt pavement management. Sci. Total Environ. 775, 145741.
Stachel, B., Holthuis, J.-U., Schulz, W., Seitz, W., Weber, W.H., Tegge, K.-T., Dobner, I., 2010. Treatment techniques and analysis of stormwater run-off from roads in hamburg, Germany. In: Fatta-Kassinos, D., Bester, K., Kümmerer, K. (Eds.), Xenobiotics in the Urban Water Cycle: Mass Flows, Environmental Processes, Mitigation and Treatment Strategies. Environ. Pollut, Springer Netherlands, Dordrecht, pp. 445–461.
Stechmann, H., Dannecker, W., 1990. Characterization and source analysis of vehicle-generated aerosols. J. Aerosol Sci. 21, S287–S290.
Sun, G., Wu, Y., Feng, X., Wu, X., Li, X., Deng, Q., Wang, F., Fu, X., 2021. Precise analysis of antimony isotopic composition in geochemical materials by MC-ICP-MS. Chem. Geol. 582, 120459.
Sutherland, R.A., 2000. Bed sediment-associated trace metals in an urban stream, Oahu, Hawaii. Environ. Geol. 39, 611–627.
Thévenot, D.R., Moilleron, R., Lestel, L., Gromaire, M.-C., Rocher, V., Cambier, P., Bonté, P., Colin, J.-L., de Pontevès, C., Meybeck, M., 2007. Critical budget of metal sources and pathways in the Seine River basin (1994–2003) for Cd, Cr, Cu, Hg, Ni, Pb and Zn. Sci. Total Environ. 375, 180–203.
Thorpe, A., Harrison, R.M., 2008. Sources and properties of non-exhaust particulate matter from road traffic: a review. Sci. Total Environ. 400, 270–282.
Turner, A., Filella, M., 2020. Antimony in paints and enamels of everyday items. Sci. Total Environ. 713, 136588.
Varrica, D., Bardelli, F., Dongarrà, G., Tamburo, E., 2013. Speciation of Sb in airborne particulate matter, vehicle brake linings, and brake pad wear residues. Atmos. Environ. 64, 18–24.
Von Uexküll, O., Skerfving, S., Doyle, R., Braungart, M., 2005. Antimony in brake pads-a carcinogenic component? J. Clean. Prod. 13, 19–31.
Wang, D., Mathur, R., Zheng, Y., Qiu, K., Wu, H., 2021. Redox-controlled antimony isotope fractionation in the epithermal system: new insights from a multiple metal stable isotopic combination study of the Zhaxikang Sb–Pb–Zn–Ag deposit in Southern Tibet. Chem. Geol. 584, 120541.
Wang, Q., Zhang, Q., Wu, Y., Wang, X.C., 2017. Physicochemical conditions and properties of particles in urban runoff and rivers: implications for runoff pollution. Chemosphere 173, 318–325.
Weckwerth, G., 2001. Verification of traffic emitted aerosol components in the ambient air of Cologne (Germany). Atmos. Environ. 35, 5525–5536.
Ye, L., Chen, H., Jing, C., 2019. Sulfate-reducing bacteria mobilize adsorbed antimonate by thioantimonate formation. Environ. Sci. Technol. Lett. 6, 418–422.
Ye, L., Jing, C., 2022. Iron(III) reducing bacteria immobilise antimonite by respiring elemental sulfur. Geochem. Persp. Lett. 21, 37–41.
Ye, L., Zhong, W., Zhang, M., Jing, C., 2021. New mobilization pathway of antimonite: thiolation and oxidation by dissimilatory metal-reducing bacteria via elemental sulfur respiration. Environ. Sci. Technol. 56, 652–659.
Zhang, H., Lombi, E., Smolders, E., McGrath, S., 2004. Kinetics of Zn release in soils and prediction of Zn concentration in plants using diffusive gradients in thin films. Environ. Sci. Technol. 38, 3608–3613.
Zhou, W., Zhou, A., Wen, B., Liu, P., Zhu, Z., Finfrock, Z., Zhou, J., 2022. Antimony isotope fractionation during adsorption on aluminum oxides. J. Hazard Mater. 429, 128317.